TAMPEREEN TEKNILLINEN YLIOPISTO
TAMPERE UNIVERSITY OF TECHNOLOGY

Somnath Dey

Benzothiazole and Perylene Bisimide Derivatives – Synthesis and Opto-Electronic Characterization

Julkaisu 1043 • Publication 1043

Tampere 2012

Tampereen teknillinen yliopisto. Julkaisu 1043
Tampere University of Technology. Publication 1043

Somnath Dey

Benzothiazole and Perylene Bisimide Derivatives –
Synthesis and Opto-Electronic Characterization

Thesis for the degree of Doctor of Science in Technology to be presented with due permission for public examination and criticism in Festia Building, Auditorium Pieni Sali 1, at Tampere University of Technology, on the 25th of May 2012, at 12 noon.

Tampereen teknillinen yliopisto - Tampere University of Technology
Tampere 2012

ISBN 978-952-15-2827-9 (printed)
ISBN 978-952-15-2858-3 (PDF)
ISSN 1459-2045

Abstract

This work investigates the tuning of photophysical properties of two different classes of photoactive molecules, 2-(2′-hydroxyphenyl)benzothiazole (HBT) and perylene bisimide (PBI). The Suzuki coupling reaction was employed to synthesize aryl-substituted derivatives of HBT and PBI. The tuning of the photophysical properties of both HBT and PBI was successfully carried out by attaching either electron-donating (ED) or electron-withdrawing (EW) aryl moieties to the parent compounds. For HBT, a series of 5-substituted derivatives were synthesized to modify the highest occupied molecular orbital (HOMO) energy levels of zinc-benzothiazole (Znb_2) complexes. Perylene *bay* substitutions were used to tune the HOMO-LUMO (LUMO: lowest unoccupied molecular orbital) energy gap of the diaryl-PBIs.

Spectroscopic and electrochemical techniques were used to determine the effects of substituents on the photophysical properties to the parent compounds. For the Znb_2 complexes, absorption and emission spectra as well as the HOMO energy levels are effectively modified by the aryl-substitution while the LUMO energy level remains largely unaffected. Whereas, for the PBI derivatives, the spectroscopic profiles as well as the HOMO and LUMO energy levels were tuned by the attached aryl groups. These results indicate that inductive effects are more dominant in both Znb_2 and PBI derivatives.

All the involved reactions, especially borylation of both the HBT and PBI were studied in detail to achieve maximum yield and simple purification. The separation of a series of 1,7- and 1,6-diaryl-PBIs by normal column chromatography was an important step in perylene chemistry. The individual regioisomers of diaryl-PBIs were unambiguously characterized by observing the chemical shifts of α-methylene protons using 300 MHz ^{1}H NMR spectroscopy. Obtained results indicate that both 1,7- and 1,6-regioisomers of same diaryl-PBI possess slightly different opto-electronic properties, which might be important while designing a system for optical devices.

Moreover, the synthesized Znb_2 complexes were used as anode buffer layers in thin film bulk-hetero junction (BHJ) based inverted organic solar cells. The presence of vacuum evaporated Znb_2 buffer layers was found to enhance the photovoltaic performance by up to 40 % when compared to a similar device containing tris(8-hydroxyquinlinato)aluminum(III) (Alq_3) buffer layer. The device stability also improved considerably when compared to the corresponding device with the Alq_3 buffer layer.

Finally, benzothiazole-perylene bisimide (HBT-PBI) dyads, in which two chromophore units were linked in close proximity to each other, were synthesized and studied by optical spectroscopy to explore a new donor-acceptor light-harvesting photovoltaic antennae system.

Preface

It is my great pleasure to express my gratitude to my supervisor, Prof. Helge Lemmetyinen for giving me the opportunity to work in his excellent and diverse group. I also thank him for keeping his faith in me during difficult times and encouraging me to study spectroscopy and solar cells besides synthesis. I appreciate all his contributions of time, ideas, and funding to make my PhD experience productive and stimulating. I also want to thank Dr. Alexander Efimov for all his help during the synthesis. I would like to express my gratitude to Prof. Nikolai Tkachenko for teaching the basics of spectroscopy. I also want to express my appreciation to all the co-authors of publications.

For the pleasant work atmosphere, I am grateful to all my colleagues in the "Supramolecular Photochemistry" group. Especially I want to thank Rajeev Dubey for all his support, advice and criticism during the last four and half years. My great appreciation goes to my colleagues in the synthetic lab, Jenni Ranta, Dr. Juha Heiskanen, Dr. Kalle Lintinen, and Essi Sariola-Leikas. I also want to thank Dr. Paola Vivo and Dr. Kimmo Kaunisto for their help during my solar cell studies. My gratitude cannot be complete without mentioning my "office-mates" for providing an excellent ambiance. I want to thank Antti Tolkki, Venla Manninen, Ali Al-Subi and Dr. Alexey Veselov for sharing life experiences and science with me.

I want to thank my friends in Finland, especially Dr. Nikhil Pratap and Dr. Veer Dhaka, and their family for treating me like a family member. Most of all, I want to thank my loving and caring parents for all the encouragement and support, even when I moved to Finland. Especially I want to thank my mother Sanchita for all the motivation. My brother, Tanmay and my sister deserve credits for all the fun I had during my visits.

This work was carried out at Department of Chemistry and Bioengineering, Tampere University of Technology between September 2007 and May 2012. I gratefully acknowledge the Academy of Finland and the Department of Chemistry and Bioengineering for funding.

Tampere, May 2012
Somnath Dey

Table of contents

Abbreviations and symbols

Alq_3	tris(8-hydroxyquinlinato)aluminum(III)
Bn	benzyl
BHJ	bulk-heterojunction
DCM	dichloromethane
DMSO	dimethyl sulfoxide
dppf	1,1'-bis(diphenylphosphanyl)ferrocene
DPV	differential pulse voltammetry
E_g	optical bandgap
E_{ox}	oxidation potential
E_{red}	reduction potential
ED	electron-donating
ESIPT	excited-state intramolecular proton transfer
Et_3N	triethyl amine
eV	electron volt
EW	electron-withdrawing
Fc	ferrocene
FF	fill factor
FTIR	Fourier transformation infrared
FWHM	full width at half maximum
HBT	2-(2′-hydroxyphenyl)benzothiazole
HBL	hole-blocking layer
HOMO	highest occupied molecular orbital
HTL	hole-transporting layer
ITO	indium tin oxide
J_{max}	maximum current density
J_{sc}	short circuit current
KOAc	potassium acetate
LUMO	lowest unoccupied molecular orbital
NaOAc	sodium acetate
NHE	normal hydrogen electrode
NIR	near infrared
NMR	nuclear magnetic resonance
OFET	organic filed-effect transistor
OLED	organic light emitting diode
OPV	organic photovoltaics

OSC	organic solar cell
P_0	input optical power
P_{max}	largest power output
P3HT	poly(3-hexylthiophene)
PBI	perylene bisimide
PCBM	phenyl C_{61} -butyric acid methyl ester
$PdCl_2(dppf)\cdot CH_2Cl_2$	[1,1'-bis(diphenylphosphanyl)ferrocene]dichloropalladium(II) dichloromethane salt
PEDOT/PSS	poly(3,4-ethylenedioxythiophene)/poly(styrene-*p*-sulfonate)
PPA	polyphosphoric acid
$TBABF_4$	tetrabutylammonium tetrafluoroborate
TBACl	tetrabutylammonium chloride
$TBAPF_6$	tetrabutylammonium hexafluorophosphate
TCSPC	time-correlated single photon counting
THF	tetrahydrofuran
U_{max}	largest output voltage
U_{oc}	open circuit voltage
UV	ultraviolet
UV- Vis	ultraviolet-visible spectroscopy
Znb_2	bis[2-(2-hydroxyphenyl) benzothiazolato]zinc(II)
ZnO	zinc oxide
1a	bis{2-[2-hydroxy-5-(2,3,5,6-tetrafluoropyridyl)phenyl]benzothiazolato}zinc(II)
1b	bis{2-[2-hydroxy-5-(2,3,4,5,6-pentafluorophenyl)phenyl]benzothiazolato}zinc(II)
1c	bis[2-(2-hydroxy-5-phenylphenyl) benzothiazolato]zinc(II)
1d	bis(2-{5-[4-(dimethylamino)phenyl]-2-hydroxyphenyl}benzothiazolato)zinc(II)
Φ_F	fluorescence quantum yield
ε	molar extinction coefficient
η	photovoltaic efficiency
λ	wavelength
τ	fluorescence life-time
υ	frequency

List of publications

The thesis is based on the work contained in the following publications, which are hereafter referred by their Roman numerals.

I. Electronic Structure Manipulation of Zinc Benzothiazole Complex: Synthesis, Optical and Electrochemical Studies of 5-substituted Derivatives

Somnath Dey, Alexander Efimov, Chandan Giri, Kari Rissanen, and Helge Lemmetyinen, *Eur. J. Org. Chem*. **2011**, 6226-6232.

II. Enhanced Performance and Stability of Inverted Organic Solar Cells by Using Novel Zinc-Benzothiazole Complexes as Anode Buffer Layers

Somnath Dey, Paola Vivo, Alexander Efimov, and Helge Lemmetyinen, *J. Mater. Chem*. **2011**, *21*, 15587-15592.

III. Bay Region Borylation of Perylene Bisimides

Somnath Dey, Alexander Efimov, and Helge Lemmetyinen, *Eur. J. Org. Chem*. **2011**, 5955-5958.

IV. Diaryl-Substituted Perylene Bis(imides): Synthesis, Separation, Characterization and Comparison of Electrochemical and Optical Properties of 1,7- And 1,6-Regioisomer

Somnath Dey, Alexander Efimov, and Helge Lemmetyinen, *Eur. J. Org. Chem.* **2012**, 2367-2374.

Author's contribution

Somnath Dey has both planned and carried out almost all of the experimental work, data analysis and written all the publications listed above.

1 Introduction

1.1 Motivation

The worldwide demand for energy has grown enormously over the last century as a consequence of the increasing rate of industrialization throughout the world. In 2010, the total global energy consumption was approximately 16 TW.[1] With the improvements of living standards across the planet, the need for energy is likely to grow even more in the 21st century; moreover, the rapid growth of developing nations like India and China, has emphasized the problem of energy demand. The projected global energy demand would be 28 TW by 2050.[2] Most of today's energy demand comes from non-renewable energy sources like oil, coal, and natural gas. Combustion of these fossil fuels has harmful effects on the Earth's ecosystem by exposing the land and sea to pollutants like carbon dioxide (CO_2), nitrogen oxides (NO_x), sulfur dioxide (SO_2), and heavy metals. As the main combustion product, CO_2 is considered to be one of the most prominent contributors to the "greenhouse effect" accelerating global warming.[3] An increase in global warming will cause an alarming sea-level rise (eliminating many small island nations), the acidification of oceans, changes in the pattern of precipitation and the encroachment of the subtropical deserts.[4] All of these will have a devastating effect on all forms of life on earth.

With respect to the ecological problems and the limited availability of fossil and nuclear fuels, special focus is on renewable energy sources to contribute significantly to the world's energy supply. But even in a best case scenario, the combined accessible capacities of water, wind, biomass and geothermal energy could supply just 22 TW in total. The sun, on the other hand provides 120, 000 TW of radiations on earth each year. In total, 36, 000 TW is shining onto landmass. A practical global solar potential value is estimated to be at 600 TW. Thus, using solar farms with an efficiency of 10 %, about 60 TW of energy can be generated.[5]

Solar energy generally converted into electricity using photovoltaics (solar cells) or thermal systems. The solar cell technologies have been experiencing a large growth in the last decade and the total capacity of installed solar cells reached 40 GW in 2010.[6] However, both photovoltaics and thermal system industries have to grow enormously in order to provide a significant fraction of the entire global energy production.

From the yearly mean of irradiance in the world, (Figure 1.1)[7] it is evident that subtropical deserts have the best potential for photovoltaic installations. However, higher latitude countries especially Nordic countries can also benefit from the fact that very long summer days can provide around-the-clock electricity generation from sunlight. Thus, the sun could be a singular solution for all our future energy needs if we know how to harvest sunlight and store the solar energy in a cost-efficient way.

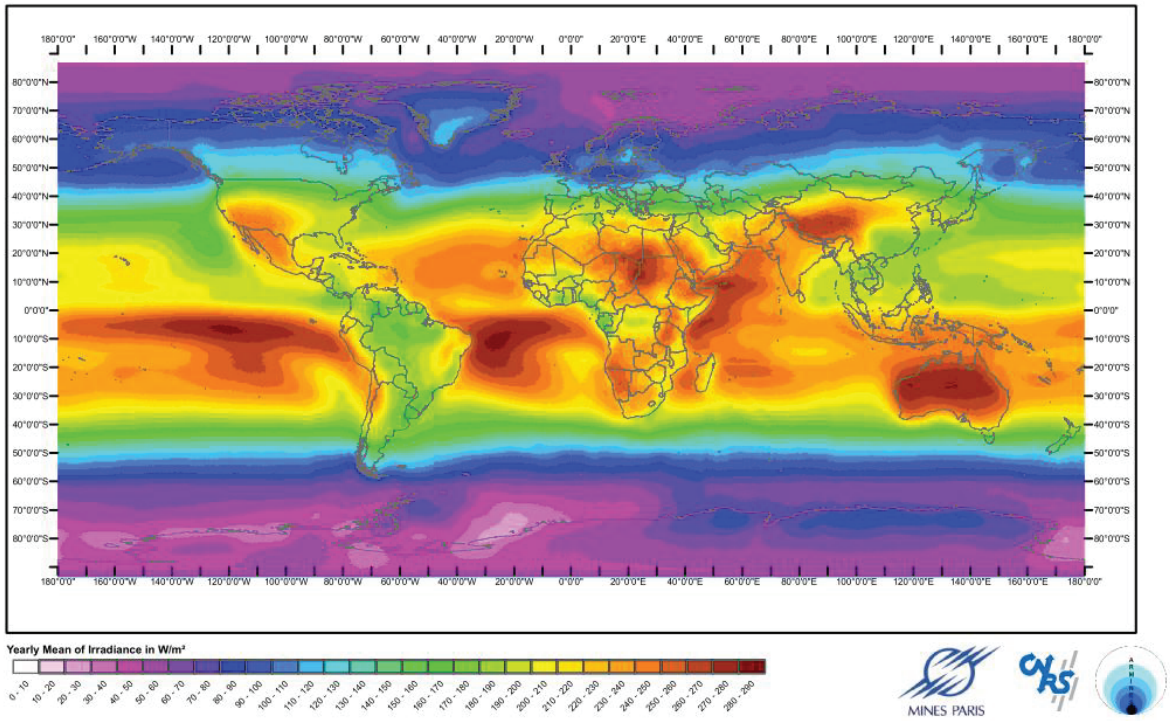

Figure 1.1. Yearly mean of irradiance in the world.[7]

To foster the growth of photovoltaic adaptation as a future source of energy, large-scale production and manufacturing cost of photovoltaic systems should be substantially reduced.[8] To overcome the main limitations of efficiency and durability of existing organic photovoltaics, it is imperative to synthesize compounds that match the solar spectrum, optimize the device architecture, and understand the photo-induced phenomena inside the thin-film structures. Hence, the synthesis of new classes of compounds and applying them in solar cells are essential for the design of efficient photovoltaic devices.

1.1 The aims and contents of the Thesis

This Thesis aims to offer a contribution to the understanding of the tuning of photophysical properties of photoactive molecules via attachment of either electron-withdrawing (EW) or electron-donating (ED) aryl groups to the photo-active compounds and to study their properties by spectroscopic and electrochemical methods. The Suzuki coupling reaction[9, 10] was used to synthesize aryl-substituted derivatives.

In the present study, a series of new compounds were synthesized, bearing either EW or ED aryl groups at the 5-position of 2-(2′-hydroxyphenyl)benzothiazole (HBT) and at the *bay* region of perylene bisimide (PBI). HBT derivatives were used to synthesize bis[2-(2′-hydroxyphenyl) benzothiazolato]zinc(II) (Znb_2) complexes.[I] Photocurrent measurements were done to test the applicability of synthesized compounds as an anode buffer layer in inverted organic solar cells (OSC).[II] All the reactions involved in the synthetic schemes were studied thoroughly,

revealing new insights. Especially the borylation of both HBT and PBI was studied in detail to gain knowledge regarding the effects of various reaction conditions on the product yield and ease of purification.[I, III] Moreover, in the case of the PBI derivatives, a series of 1,7- and 1,6-regioisomers of diaryl-substituted PBIs were isolated via conventional column chromatography, which has previously not been succeeded.[IV] Finally, HBT-PBI dyads were synthesized as they might behave as a light-harvesting antenna in photovoltaic applications.

Steady-state spectroscopy and time-resolved measurements were used to determine the effect of various aryl groups in the parent compound. Electrochemical methods were used to measure the redox potentials and to calculate the molecular energy levels of each derivative.

The following chapters will provide background reading to the papers, a summary from the results, and an outlook for the future work:

- The properties and current state of development of OSCs; in particular, the working principles of OSC, photo-active materials, and coupling reactions will be introduced in Chapter 2.
- Chapter 3 describes a short introduction to the classes of compounds used in this study, the instrumentation involved for their characterization, and for spectroscopic, electrochemical, and photocurrent measurements.
- Chapter 4 describes all the synthetic, spectroscopic, electrochemical, and photocurrent results from this work, and also provides an outlook for the future.
- Finally, chapter 5 summarizes the conclusions based on the synthetic and spectroscopic results.

2 Background

2.1 Evolution of organic solar cells

Conversion of solar energy into electrical power through the so-called "photovoltaic effect" can be traced back to Edmond Becquerel's (1839) pioneering work with liquid electrolytes.[11] Becquerel observed generation of a photocurrent when platinum electrodes covered with silver chloride or silver bromides were illuminated in aqueous solution (electrochemical cell). Since that it has been the basis for various concepts developed to convert solar energy to electricity. However, the biggest impact on the solar cell technology was achieved more than one century later by Chapin et al. (Bell Laboratories) in 1954.[12] They converted solar radiation into electricity in a silicon-based single *p*-*n* junction device with a power conversion efficiency of 6 %. The *p*-side contained an excess of positive charges (holes), and the *n*-side an excess of negative charges (electrons). An electric field formed in between these two layers and the electrons and holes, created through the light absorption of Si, diffused through the layer, where they were accelerated by the electric field and collected by the opposite electrodes.

Over the years, many improvements have been achieved in terms of the efficiency and the stability of photovoltaic devices. The highest efficiency achieved with a single crystal Si cell is 25 %.[13] Recently, with a tandem cell approach (stacking of several devices in series), an efficiency of 40.8 % has been achieved.[14] It is, however, important to emphasize that the efficiency of most of the commercial inorganic solar cells lies between 14-19 %, which is much lower than the highest efficiency achieved in controlled laboratory conditions. Moreover, efficiency improvements often result in additional costs arising from manufacturing the devices from ultra-pure rare materials and complex device architectures. Thus, for mass production, it is mandatory to reduce the cost-to-performance ratio as much as possible.

In spite of the promising efficiencies of conventional inorganic solar cells, high up-front cost prevents its large-scale applications. The limited natural resources of some of the crucial elements like tellurium, gallium and indium, also poses a major problem for using the latest highest performing inorganic cells for mass productions.[15]

Organic semiconductors are a less-expensive alternative to inorganic semiconductors like Si. Unlike their inorganic counterparts, organic molecules can also be mass processed at a lower temperature. The thin-film solar cells are flexible and lightweight, which can lead to innovations such as solar shingles, panels that can be rolled out onto any surface, consumer products, or even integrated into the building architecture.[16-18] Moreover, the ability to tune the physical properties of organic molecules by modifying their chemical structure constitutes the main drivers

boosting research and industrial interests in OSCs. The efficiencies of modern OSCs lie in the range of 6-13 %.[19] Despite many improvements over the years, OSCs have not yet reached the market place similar to inorganic solar cells but the future is certainly looks bright for OSCs.[20]

In the last three decades, at the cutting age third generations OSCs evolved are: (i) dye-sensitized solar cells (DSSC) pioneered by M. Grätzel in 1991,[5, 21] which are essentially electrochemical cells composed of TiO_2 covered with molecular dye (generally Ru-complexes); (ii) multi-junction cells;[22] (iii) hybrid solar cells, in which inorganic nano-crystals or quantum dots are doped into a polymer matrix;[23] (iv) small molecule and polymeric solar cells.[24, 25] This Thesis focuses only on the latter approach.

While the efficiencies of OSCs are steadily improving, mainly due to the advent of new low bandgap polymers, the stability of the devices remains poor.[26] Conjugated polymers and fullerene derivatives are highly sensitive to photo-oxidation.[27] Fullerene derivatives also exhibit low conductivity upon oxygen absorption.[28] Thus, it is necessary to encapsulate the solar cell by preventing the exposure of active materials to oxygen and water vapor. Moreover, in un-encapsulated devices prolonged exposure to atmosphere can lead to oxidation of the metal electrode by the formation of an insulating oxide layer.[29] Hence, long-term durability of the devices without encapsulation is essential to reduce the costs of the technology. At the present, the longest reported lifetime of OSCs is over one year in outdoor conditions.[30]

2.2 Basic working principles of organic solar cells

In organic solar cells, conversion of incident light into the electric current is accomplished by four consecutive steps: (i) *absorption* of a photon leading to the formation of an excited state, the electron-hole pair (*exciton*), (ii) *exciton diffusion* to a region, where (iii) the *charge separation* occurs, and (iv) the *charge transport* to the anode (holes) and cathode (electrons), to supply a direct current (Figure 2.1).[16, 31-34]

Using strategies to maximize each step, the performance enhancement of an OSC cell can be effectively achieved. The following points describe each conversion step and the losses involved in those steps:

(i) *Absorption* of photons: In most of the organic devices, only a small portion of the incident light gets absorbed, because the semiconductor bandgap (HOMO-LUMO energy) is too high. A semiconductor bandgap of 1.1 eV (1100 nm, $\Delta E = 1240/\lambda$) is required to absorb ~ 75 % of solar radiation, whereas, most of the polymer has a bandgap higher than 2 eV, which limits possible absorption to about 30 %.

(ii) *Exciton diffusion*: After the photon absorption, organic semiconductors produce excitons. As excitons are neutral species and strongly bound electron-hole pairs, their motion is not influenced by any electric field. Excitons are generally diffused via random hops; importantly, prior to their decay back to ground state. The typical exciton diffusion length for organic semiconductors is ~ 10-20 nm,[35] and due to the offset of HOMO energy levels of donor and acceptor, the exciton dissociation occurs only at the donor-acceptor interface. If excitons do not reach the

interface, they recombine and the absorbed energy is dissipated without generating photocurrent. Therefore, to generate power, the excitons have to be dissociated and collected at electrodes before recombination.

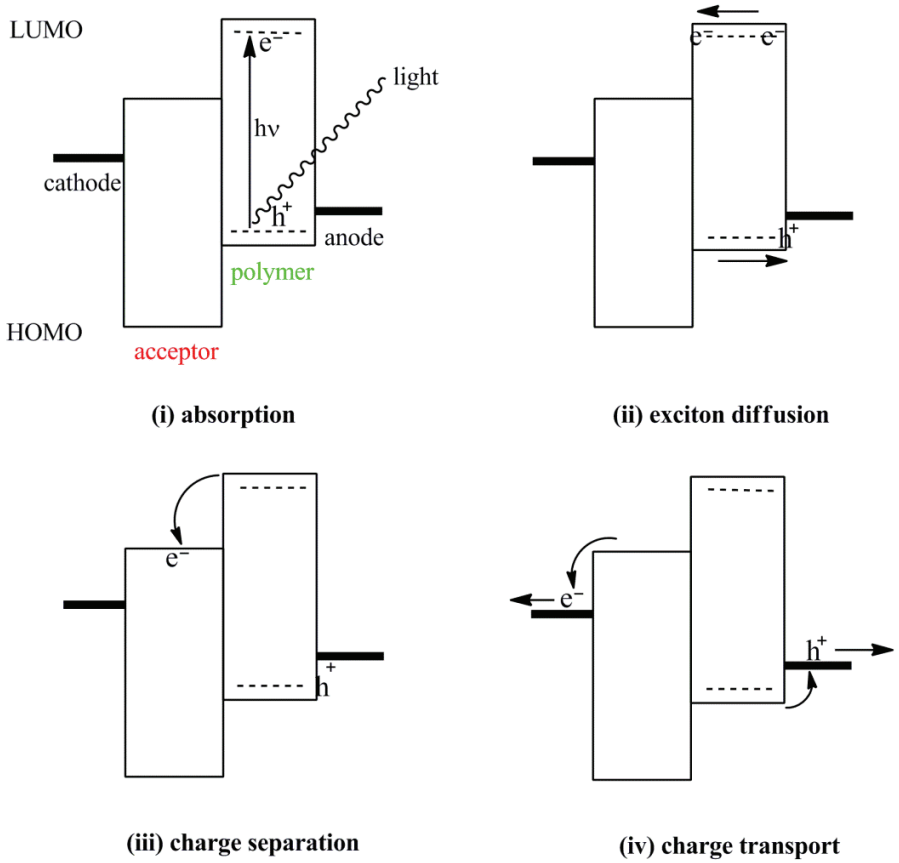

Figure 2.1. Schematic picture describing the conversion steps in organic solar cells.[33] HOMO: highest occupied molecular orbital, and LUMO: lowest unoccupied molecular orbital.

(iii) *Charge separation*: Charge separation usually occurs at the semiconductor/electrode interfaces. If the work-functions of the electrodes were not suitable enough to overcome the exciton binding energy (~ 0.4 eV),[36] charge transfer may occur, but the exciton does not split into their constituent charges and recombine at the donor-acceptor interface.

(iv) *Charge transport*: The transport of charges is affected by recombination during the journey to the electrodes and may be interaction with atoms and other charges. Both the exciton and charge transport in organic materials usually require hopping from molecule to molecule. Thus, close packing of the molecules is assumed to decrease the width of the intermolecular barriers and a planar molecular structure should generally lead to better transport properties than bulky three-dimensional molecules.

2.3 Basic organic solar cell architectures

The differences between the existing organic solar cell architectures lie mainly in the exciton dissociation process, which can occur in different locations, based upon the device architecture. The most widely investigated small molecule or polymeric solar cells are:

(i) Single layer solar cells, based on a single organic layer (typically evaporated), sandwiched between two electrodes with different work-functions.[31] These solar cells are very inefficient, due to the small exciton diffusion length of most of the organics, which limits photo-generation to take place in a thin layer near the interface.[25]

(ii) Bi-layer hetero junctions are bi-layer devices, where a donor material and an acceptor material are stacked together to form a hetero junction, and which is then sandwiched between two electrodes.[37] A big advantage of bi-layers compared to single layer cell is that charges formed after exciton diffusion, i.e. electrons can travel through an *n*-type acceptor, and holes can travel through *p*-type material, which greatly reduces the possibility of charge recombination.[38]

(iii) Bulk-hetero junction (BHJ) solar cells, for which the donor and acceptor materials are intimately mixed to form an interpenetrating network.[39, 40] As a result, efficient exciton diffusion occurs within the bulk, but at the separate donor and acceptor phases.[41, 42] Currently, BHJ cells are most efficient and they can be combined with cheap and easy device fabrication technology.[43] This Thesis solely concentrates on studies of BHJ cells, as they are the most promising in this field.

In most organic solar cells, the front electrode is based on a transparent conducting oxide, such as indium tin oxide (ITO), that serves as the high work-function, positive electrode.[44] To achieve the built-in electric field needed for device to operate, the back electrode must be made from a low work-function metal (usually Al) that serves as the negative electrode. In the operation of the typical polymer-fullerene derivative blend BHJ solar cell, electrons generated in the active layer are collected by the Al electrode, and holes are collected by the ITO. In such a device, without sophisticated encapsulation to prevent an exposure to atmosphere, the facile oxidation of the low work-function metal represents an inherent instability.[26, 29] However, the cell polarity can be reversed by inserting a hole-blocking layer (HBL) between the ITO and the active layer (usually a ZnO layer), so that only electrons can reach the ITO, and the metal electrode must become the hole-collecting positive electrode (see Figure 2.2).[45] It can then be made from a high work-function metal that is more air-stable.[46] This kind of "inverted" structure provides higher flexibility to the design of multi-junction or tandem polymer solar cells.[47, 48] Moreover, the inverted structure removes the need for a ITO-side hole-transporting layer (HTL), generally poly(3,4-ethylenedioxythiophene)/ poly(styrene-*p*-sulfonate) (PEDOT/PSS), which is believed to introduce chemical and morphological instabilities at the interface with ITO.[49] Inverted OSC architecture has been studied in this Thesis and in publication II.

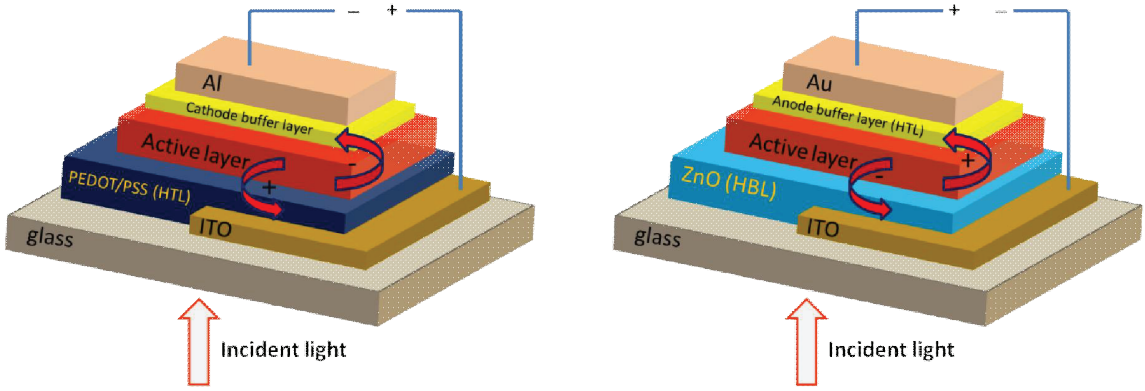

Figure 2.2. Normal architecture of a conventional (left) and inverted organic solar cell (right).

2.4 Photoactive molecules in organic solar cells

Plants use the natural process of photosynthesis to convert sunlight into chemical energy, where in the first step, the chlorophyll molecules absorb the sunlight. Interestingly, chlorophyll pigment and its analogous molecules can be directly applied in a single layer solar cell.[38] Materials having a delocalized electron system can absorb sunlight, create photo-generated charge carriers, and transport these charge carriers.

Porphyrins and phthalocyanines are less stable and less synthetically tractable chlorophylls, which are common electron and energy donors in naturally occurring photosynthesis (Figure 2.3).[50] Porphyrins have a highly conjugated macrocyclic structure (22 π-electrons), producing intense absorption in the visible region (strong band ~ 400-450 nm, Soret band). Phthalocyanines are structural analogues of porphyrins. The main difference to porphyrins is that in phthalocyanines the four pyrrole units are benzo-fused to form isoindoles and are connected via aza-bridges. Phthalocyanines have a Soret band and intense Q-bands in the red-part of the solar spectrum (620-700 nm). Both porphyrins and especially phthalocyanines are used in organic photovoltaics, because of the better matching of their absorption spectrum with that of the sun.[51]

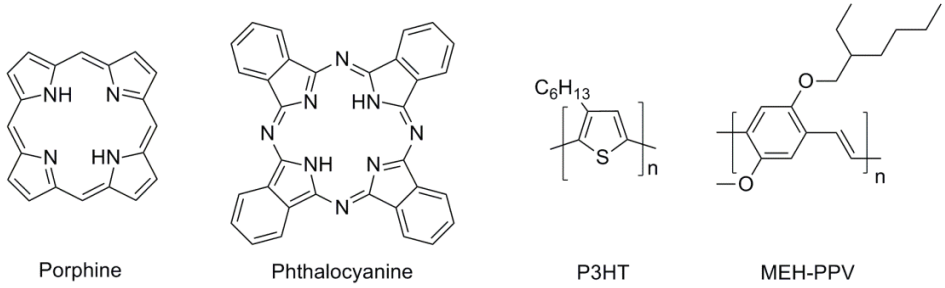

Figure 2.3. Molecular structure of porphine, phthalocyanine, P3HT and MEH-PPV.

Poly(*p*-phenylene vinylenes) (PPV) and polythiophenes are the most common conducting polymers used in OSC. Poly(3-hexylthiophene) (P3HT) is a widely studied electron donor material due to its excellent change transport

properties. It also absorbs in a wide part of the solar spectrum, between 400-650 nm.[52] Blends of P3HT and fullerene or its derivatives are the most widely studied configurations for OSCs. PPV and its derivatives are also extensively used, because conductivity of PPV increases several orders of magnitude in the presence of atmospheric oxygen, which favors electron abstraction from *p*-type donor PPV.[53]

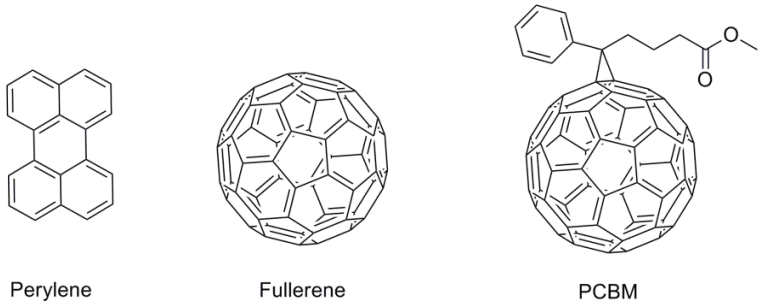

Figure 2.4. Molecular structure of perylene, fullerene and PCBM.

Fullerene and perylene are the most commonly used acceptor materials in opto-electronic applications (Figure 2.4).[54] Fullerenes are even-numbered clusters of carbon atoms in the range of C_{30}-C_{100}.[55] The most stable structure of fullerenes is the one consisting of 60 carbon atoms, i.e. C_{60} or buckminsterfullerene. Fullerenes are very special class of molecule because of their high symmetry, high electron-affinity,[56] and ability to stabilize negative charges.[57] These exciting properties of fullerenes have led to synthesis and study of a wide-range fullerene derivatives in the last two decades.[50] Fullerene derivative phenyl C_{61}-butyric acid methyl ester (PCBM) is currently the most commonly used acceptor in OSCs. Perylene will be discussed in section 3.1.2.

2.5 Buffer layer

The dramatic improvement of overall OSC performance registered in the last decade has been mainly due to the combination of optimized active layer nanoscale morphology and improved electronic properties of donor polymer. However, the performance of a polymer solar cell, and in general, any OSC, is also affected by the quality of the device electrodes, which contributes considerably to the overall efficiency. In order to improve the device performance and stability, a thin interlayer is commonly used between the active layer and the electrodes. This additional interlayer, known as “buffer layer”, is no longer considered optional, but is essential for achieving maximum performance.[58, 59] Every single-junction OSC nowadays includes both an anode buffer layer and a cathode buffer layer, as shown in Figure 2.2.

A large number of electrode buffer layers have first been established for organic light-emitting diodes (OLEDs) and later on have been transferred to the OSC devices. The role of buffer layers can be summarized in the following points: (i) they strongly affect the properties of the organic/electrode interface by inducing interfacial charge distribution, geometry modifications;[60] (ii) they protect the active layer from the diffusion of top electrode material through the active layer; and (iii) they can even act as an oxygen and water vapor blocker.[58] Electrode buffer

materials are mainly selected based on their molecular energy levels and charge transport properties. Moreover, electrode buffer layers are necessary for reversing the cell polarity, as for inverted OSC devices, in which glass|ITO is also being commonly used as a substrate.[60] In this Thesis, ZnO was used as cathode and Znb_2 complexes as anode buffer layers.[II] In the following two sections, the main characteristics of the cathode and anode buffer layers are briefly described.

2.5.1 Cathode buffer layer

The role of the cathode buffer layer is to improve the cathode electrode efficiency in collecting and extracting the charge carriers. As the commonly used acceptor, fullerene derivatives have high electron affinity,[56] cathodes with a high work-function electrode, like Au or Ag, is generally required for OSCs. Moreover, the work-function of cathodes mainly affects the open-circuit voltage. Additionally, maximum performance is achieved when the work-function of a cathode is aligned with the LUMO level of the acceptor.[61] Thus, a good cathode buffer layer should have the following properties: (i) to provide an ohmic contact with the acceptor material; (ii) to carry electrons efficiently; (iii) to block holes (to prevent leakage current); (iv) to be thermally and photo-chemically stable; and (v) to be transparent in case of inverted OSC devices.

Usually alkali metal compounds (e.g. LiF,[62] Cs_2CO_3[63]), metal oxides (e.g. ZnO,[64] CaO,[65] TiO_x,[66] Al_2O_3[67]), organic compounds (e.g. bathocuproine,[59] polyethylene oxide[68]), or self-assembled monolayers[69] are used as a cathode layer in OSC devices.

2.5.2 Anode buffer layer

The role of an anode buffer layer is to improve the anode electrode efficiency and to extract the positive carriers. As polymer materials are commonly used as donor material in OSC devices, the HOMO level of the polymer should be aligned with the work-function of the anode for an efficient ohmic contact.[61] Moreover, like the cathode, anode work-function also affects the open-circuit voltage; hence the HOMO level of the anode buffer layer is important for efficient charge collection. Thus, the main requirements for an anode buffer layer are: (i) to provide ohmic contact with donor material; (ii) to carry holes efficiently; (iii) to block electrons; (iv) to be thermally and photo-chemically stable; and (v) to be transparent in case of conventional OSC devices.

Most commonly used anode buffer layers are PEDOT/PSS,[70] metal oxides (e.g. V_2O_5,[71] MoO_3[64]), or self-assembled monolayers.[72] In the Thesis, Znb_2 complexes were used as an anode buffer layer in the inverted OSC devices.

2.6 Importance of individual molecular energy levels in organic solar cells

The molecular energy levels (HOMOs and LUMOs) and thus, the bandgap of photoactive molecules, are the most important characteristics for determining the feasibility and performance of any photovoltaic device.[25, 31, 38, 52] The schematic energy levels and inter-correlated parameters are shown in Figure 2.5.

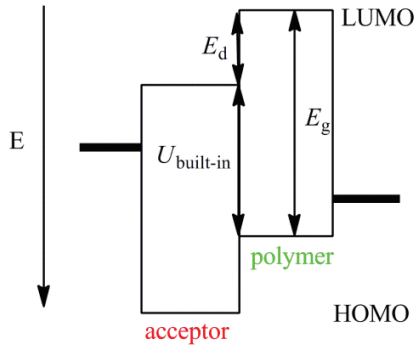

Figure 2.5. Energy diagram of donor and acceptor HOMO-LUMO levels showing linear relationship between optical bandgap E_g, LUMO energy difference E_d, built-in potential $U_{built-in}$, and molecular energy level.

In the first steps of the photovoltaic mechanism, photoactive molecules absorb sun light to convert light into electricity. The maximum photon flux density of the solar spectrum is located at 680 nm, which corresponds to a bandgap of 1.77 eV.[38] To fully exploit the solar energy, donor materials (polymer in the case of BHJ) need to absorb the red and near infrared (NIR) regions of the solar spectrum. Thus, it is highly desirable to synthesize a polymer with broader absorption through narrowing the optical bandgap without sacrificing the exciting coefficient and charge transport properties. The most straight-forward way to reduce the bandgap is to simply lower the LUMO level or raise the HOMO level of the polymer. Through numerous manipulations, polymers with a bandgap as small as 0.5 eV have been achieved.[73] Unfortunately, the availability of low bandgap polymers is not the sole determining factor for improving the performance of polymer solar cells. Following the photo-excitation, the excitons must diffuse to the donor-acceptor interface to achieve efficient change separation. It is also shown that open-circuit voltage, U_{oc}, depends linearly on the built-in potential, defined as a difference between the HOMO of donor and the LUMO of an acceptor.[74] To obtain high efficiencies, the LUMO energy level of the acceptor should also be at least 0.3 eV lower than that of the donor material to achieve energetically favorable electron transfer and overcome the binding energy of the intra-chain exciton.[75] Theoretically, on the other hand, a donor with a lower HOMO will produce maximum U_{oc}, but the LUMO of donor cannot be lower than that of the acceptor. U_{oc} of a BHJ solar cell can be empirically described as:[41]

$$U_{oc} = \frac{1}{e}\left(|E_{HOMO}^{donor}| - |E_{LUMO}^{acceptor}|\right) - 0.3, \tag{2.1}$$

where, 0.3 is an empirical factor, which relates the coulomb interaction between holes and electrons. Finally, to generate electricity, holes and electrons need to be collected at the anode, so work-function of the electrodes or energy levels of the buffer layers are important for efficient charge collection. Moreover, U_{oc} is also believed to be influenced by the work-function of the electrode,[76] which is effectively modified by the buffer layers.[77] As a result, not only polymer with a lower bandgap is needed, but molecular energy levels of all the components must also be tuned to produce maximum photovoltaic efficiency.

2.7 Coupling reactions

The coupling reaction can be described as a variety of reactions, in which a hydrocarbon fragment can be coupled with another hydrocarbon, or with other functional groups, with the aid of a metal catalyst. Cross coupling reaction is used for a wide range of C-C, C-H, C-N, C-O, C-M bond-forming processes.[78, 79] Generally, an organometallic compound of type R_1-m reacts with an organic halide R_2-X forming a new R_1-R_2 bond (Equation 2.2).

$$R_1\text{-m} + R_2\text{-X} \xrightarrow{\text{catalyst [M]}} R_1\text{-}R_2 \qquad (2.2)$$

where, m = Li (Murahashi reaction)
= B (Suzuki coupling)
= Zn (Negishi coupling)
= Si (Hiyama-Hatanaka coupling)
= Si (Stille coupling) …..

[M] = Fe, Ni, Cu, Pd, Rh …..

X = I, Br, Cl…

Since the discovery of the coupling reactions in the 1960s and 1970s, coupling reactions are continued to be one of the most widely explored branch in organic chemistry. The coupling reaction nowadays is an integral part of almost every natural product or functional molecule synthesis.[10] In 2010, the *Nobel Prize* in *Chemistry* was awarded to Ei-ichi Negishi, Akira Suzuki, and Richard F. Heck for their discovery and development of various coupling reactions.

2.7.1 Suzuki coupling reaction

The cross coupling of an aryl- or vinyl-boronic acid derivative with an organic electrophile in the presence of a base and a Pd^0 catalyst is commonly known as the Suzuki coupling reaction,[80] and has been established as a powerful tool for C-C bond formation over the past two decades. It is widely used to synthesize substituted biphenyls and poly-olefins, or in polymerization reactions.[9]

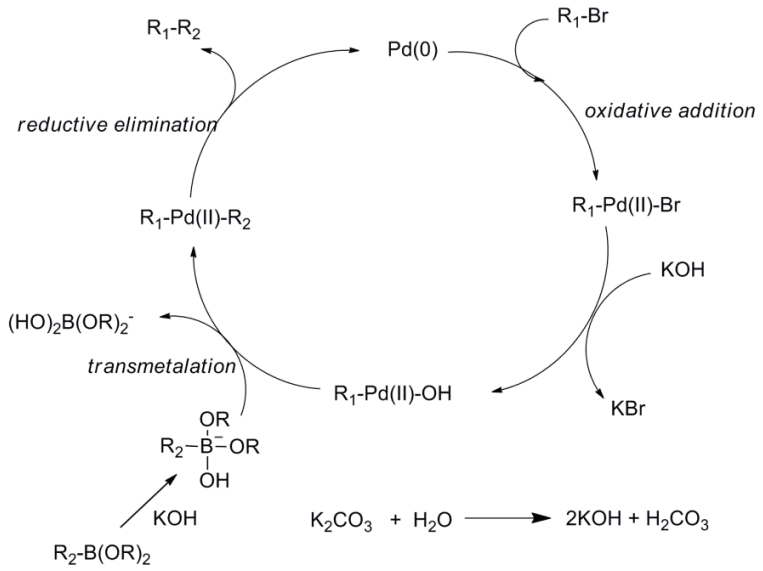

Scheme 2.1. Catalytic cycle for Suzuki coupling reaction.

A general catalytic cycle for the Suzuki coupling involves: (a) an *oxidative addition* of organic electrophile (organic halides) to the catalyst; (b) a *transmetalation* between Pd-X and R_2-B; and (c) a *reductive elimination* of the coupled product to regenerate the Pd^0 complex (Scheme 2.1).[81] Although each step involves further knotty processes, including ligand exchange, *oxidative addition* is often the rate-determining step in the catalytic cycle. The relative reactivity decreases in the order of I > Br >> Cl.[9] Aryl-halides with EW groups also facilitate *oxidative addition* when compared to those with ED groups.

A very wide range of Pd^0-catalysts can be used for the Suzuki reaction. $Pd(PPh_3)_4$ is most commonly used as catalyst, but $PdCl_2(PPh_3)_2$ and $Pd(OAc)_2$ with phosphine ligands are also efficient, since they are air-stable and readily reduced to the active Pd^0-complexes. Pd-complexes with fewer than four phosphines, a weakly coordinating ligand, or bulky phosphines, provide highly reactive catalysts because of the ready formation of the coordinatively unsaturated species.[82]

The Suzuki coupling, in general, requires the presence of a negatively charged base, such as sodium or potassium carbonate, phosphate, and hydroxide (1-2 equivalents), which used as aqueous solution. Fluoride salts such as CsF and Bu_4F are mild bases accelerating the coupling reaction of such substrates sensitive to bases.[83] The side reactions causing undesirable byproducts mainly are homo-coupling, dehalogenation, proto-deboronation reaction, and head-to-tail coupling.[84]

2.7.2 Borylation reaction

Aryl- or vinyl-boronic acid/ester derivatives are very interesting because of their usefulness in the widely used Suzuki coupling reaction to form C-C bond,[85] their biological activity,[86] and their molecular recognition

properties.[87, 88] Usually, organo-halides react with boron derivatives in presence of a base and a Pd^0-catalyst to synthesize organoboronates (Equation 2.3).

$$R_1\text{-}X + B \xrightarrow{Pd^0,\ base} R_1\text{-}B \qquad (2.3)$$

A general catalytic cycle for borylation reaction involves: (a) an *oxidative addition* of organic halides to the Pd^0-complex; (b) a *transmetalation* between Pd-X and B; and (c) a *reductive elimination* of R_1-B to regenerate the Pd^0-complex (Scheme 2.2).[9] Aryl-halide with EW groups often results in faster reaction than those with ED groups, due to their rate-determining role in the *oxidative addition*.

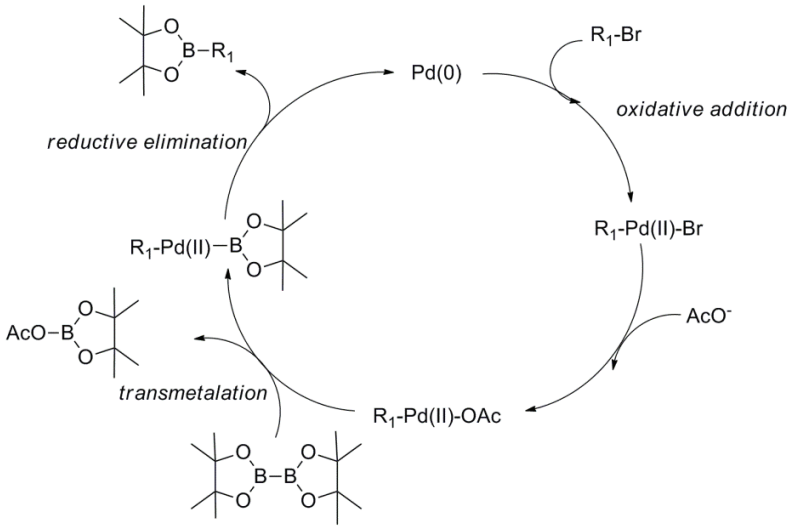

Scheme 2.2. Catalytic cycle for borylation reaction.

A wide range of Pd^0-catalysts can be used for the borylation reaction. $Pd(PPh_3)_4$ is most commonly used as catalyst, but $PdCl_2$(dppf) (dppf = 1,1'-bis(diphenylphosphanyl)ferrocene) is better, because palladium-triphenylphosphine complexes often yield byproducts derived from the coupling of the diboron with a phenyl group on triphenylphosphine in the reaction of ED aryl halides.

Stronger bases, such as K_3PO_4 and K_2CO_3, usually promote further reaction of organoboranes to form homo-coupling products via the Suzuki reaction.[9] So, weaker bases, such as potassium acetate (KOAc), sodium acetate (NaOAc), and triethyl amine (Et_3N) are generally used in the borylation reaction. The solvent also plays an important role in the rate of the homo-coupling. Borylation reaction is usually accelerated in polar solvents: e.g., DMSO ≥ DMF > dioxane > toluene.[89]

3 Materials and methods

The experimental aspects of the work are described in this section, including the classes of the compounds used in synthesis and the instruments used to characterize the products, especially instruments those were relevant for determining the structure of the molecule, spectroscopic and electrochemical properties of the synthesized compounds. The instrumentations regarding the photocurrent sample preparation and analysis are also discussed.

3.1 Compounds

Three main target molecules, 5-substituted (benzothiazole)zinc complex derivatives, bis-substituted perylene bisimide derivatives, and benzothiazole-perylene bisimide dyads were synthesized in this work. The designs and syntheses of the molecules are presented in chapter 4.1.

3.1.1 Benzothiazole

Since the pioneering work of Tang et al. in 1986 demonstrated the use of the metal complex tris(8-hydroxyquinolinato)aluminium(III), (Alq_3) as an emissive and electron transporting layer in OLEDs,[37, 90] numerous other metal complexes have been synthesized and intensively explored for OLEDs and other organic semiconductor devices.[91] Even though Alq_3 is most prominent of all the metal complexes used in organic semiconductor devices, bis(2-(2'-hydroxyphenyl)benzothiazolato)zinc(II) (Znb_2; Figure 3.1) has been proposed as a better alternative, owing to its high fluorescence efficiency, good electron transport capability, low lying HOMO (~ -5.7 eV), high thermal stability, and ease of fabrication by vacuum deposition technique.[92-95] Znb_2 has been studied as an excellent white-light emitter in OLED devices.[94, 96, 97]

The Znb_2 complex also exhibits charge transport properties,[98] which make it favourable to use as an the anode buffer layer inverted OSCs. Dimer formation in the vacuum deposited amorphous films with a close intermolecular π-π interaction of 3.7653 Å suggests a potential reason for the charge transport properties.[93]

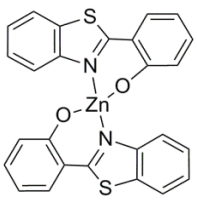

Znb_2

Figure 3.1. Structure of bis(2-(2'-hydroxyphenyl)benzothiazolato)zinc(II) complex.

Moreover, the ligand HBT exhibits excited-state intramolecular proton transfer (ESIPT) phenomena (Figure 3.2), which is also another motivation for synthesizing a series of HBT derivatives.[99-102]

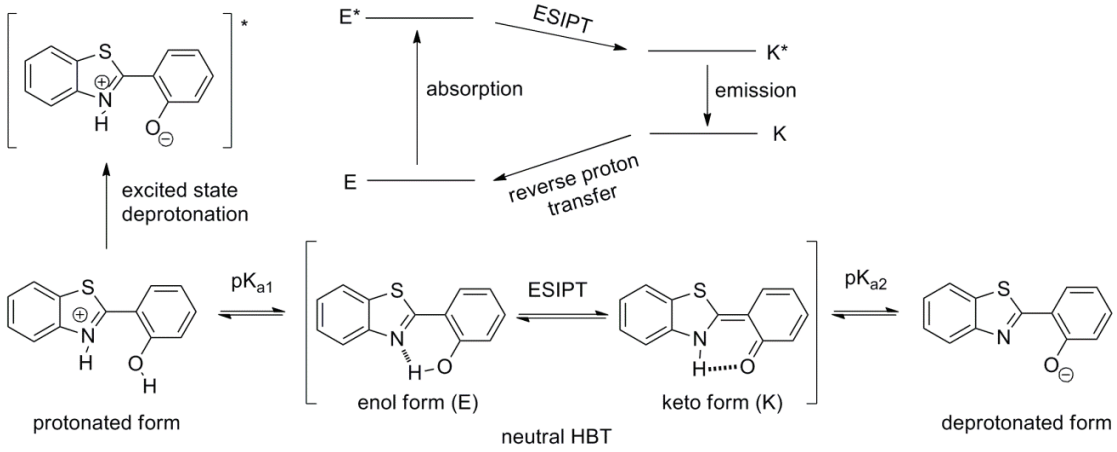

Figure 3.2. Prototropic equilibria and intramolecular proton transfer of HBT.

3.1.2 Perylene bisimide (PBI)

Perylene dyes were first discovered by Kardos in 1913,[103] and since that have been used extensively as industrial dyes and pigments.[104, 105] Perylene is a conjugated planar molecule consisting of two naphthalene molecules connected by two carbon-carbon bonds with sp^2-hybridized electronic orbitals of all the carbon atoms.[106] Extended conjugation results in a strong absorption of perylene and its derivatives in the visible part of the solar spectrum. The planar structure also leads to strong π-π stacking and thus, poor solubility in commonly used organic solvents.[107, 108] Near unity fluorescence quantum yield, strong electron accepting character, and high photochemical stability allow PBIs to be used in many newly developed applications. In the field of electronic materials, PBIs are now considered as one of the best *n*-type semiconductors available.[54, 109] To date, PBIs and its derivatives have been utilized in various opto-electronic applications, e.g. in organic field-effect transistors (OFETs),[110] dye lasers,[111, 112] OLEDs,[113, 114] organic photovoltaics,[115, 116] electro-photographic devices,[117] fluorescence solar collectors,[112] and optical power limiting devices.[118]

Because of the poor solubility of perylene dyes, the high fluorescence nature and photo-stability of perylene were not recognized until 1959.[107] Improving the solubility and tuning the optical properties of perylene are the two major challenges that perylene chemists are facing before it can be used in opto-electronic applications. PBIs with different chemical and physical properties have been obtained by modification either in the *imide N,N'*-positions or in so-called "*bay*" positions (1-, 6-, 7-, and/or 12-positions of perylene core; Figure 3.3).[108]

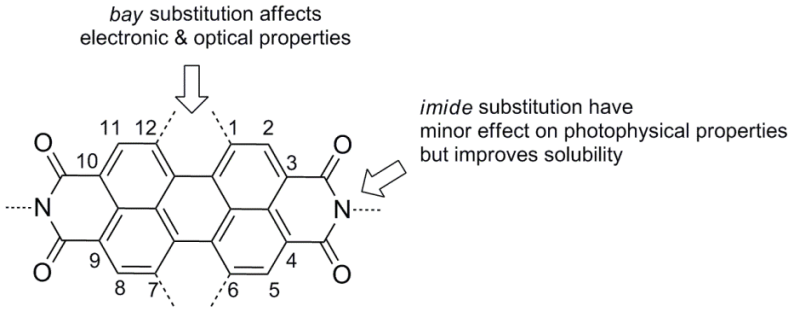

Figure 3.3. Chemical structure of perylene bisimide, and its different functional regions.

The *imide* substitution generally improves the solubility of PBIs in common organic solvents and also affects the π-π aggregation, but nevertheless, the substituents have a minor influence on the photophysical properties, because the nodes of the HOMO and LUMO orbitals are located at the *imide* nitrogens.[107, 108] In contrast, the *bay* substitution not only improves the solubility but can also have profound effect on the photophysical properties.[108, 119] As the *bay* substituents are being forced out of the perylene plane by the *bay*-hydrogens through steric interactions, which disrupt face-to-face π-π stacking, leading to improved solubility also for *bay*-substituted perylene derivatives.[120] The presence of bulky *bay*-substituents can increase the solubility by several orders of magnitude.[121] Thus, the *bay* substitution appeared more attractive and was used in this Thesis to synthesize various functional PBI derivatives.

3.2 Characterization techniques

Characterization of the products after synthesis is one of most important issue in organic chemistry. Even though there are numerous available methods to elucidate the structure of a compound, *proton* NMR (nuclear magnetic resonance) is certainly the most valuable method, not only to ascertain the structure but to also check the purity of a compound. Fourier transform infrared spectroscopy (FTIR) is another method used when it is not possible to measure NMR. Although mass spectroscopy and elemental analysis methods were also used frequently, only the NMR and FTIR methods are described here.

3.2.1 Nuclear magnetic resonance (NMR) spectroscopy

NMR is a powerful, non-selective analytical tool that enables researchers to ascertain molecular structures, including relative configuration, comparative and absolute concentrations, and even intermolecular interactions without the destruction of the analyte. NMR is a physical phenomenon in which magnetic nuclei in a magnetic field absorb and re-emit electromagnetic radiation. This energy is at a specific resonance frequency, which depends on the strength of the magnetic field and the magnetic properties of the isotope of the atoms. The resonance frequency of a particular substance is directly proportional to the strength of the applied magnetic field. If a sample is placed in a non-uniform magnetic field, the resonance frequencies of the sample's nuclei depend on where in the field they are located. Since the resolution of the imaging technique depends on the magnitude of the magnetic-field gradient, many efforts are made to develop increased field strength, often using superconductors.[122-124]

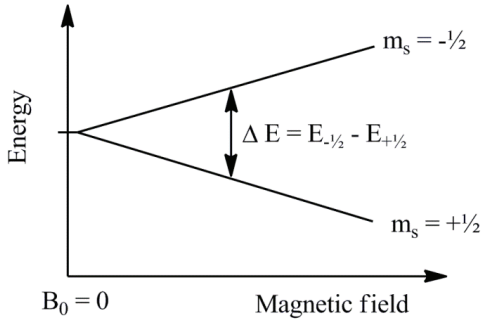

Figure 3.4. Splitting of nuclei spin states in an external magnetic field.

All isotopes that contain an odd number of protons and/or neutrons have an intrinsic magnetic moment and angular momentum, in other words, a nonzero spin, while all nuclides with even numbers of both have a total spin of zero. The most commonly studied nuclei are ^{1}H (*proton* NMR) and ^{13}C (*carbon* NMR). Nuclei from isotopes of many other elements (e.g. ^{11}B, ^{19}F, ^{31}P) have also been studied by high-field NMR spectroscopy.

All the NMR measurements presented in this Thesis were recorded with Virian Mercury 300 MHz spectrometer in deuterated chloroform ($CDCl_3$) at room temperature.

3.2.2 Fourier transform infrared (FTIR) spectroscopy

FTIR is basically an absorption spectroscopy, which deals with the infrared region of the electromagnetic spectrum, i.e. wavelengths longer than visible light (> 800 nm). The most commonly used spectrum range (4000-400 cm^{-1}) provides information on fundamental vibrations and associated rotation-vibrational structure of molecules.[125] IR spectroscopy exploits the fact that molecules absorb specific frequencies that are characteristic of their structure. These absorptions have resonant frequencies of the absorbed radiation, which match the frequencies of the bond or

the group that vibrates. The energies are determined by the shape of the molecular potential energy surfaces, the masses of the atoms, and the associated vibronic coupling. In order for a vibrational mode in a molecule to be "IR active", it must be associated with changes in the dipole. A permanent dipole is not necessary, as the rule requires merely a change in dipole moment. In this Thesis only the KBr pellet method is used for sample preparation.[I]

3.3 Spectroscopic measurements

Spectroscopic methods refer here to measurements related to the interaction of matter with light. The wider definition of spectroscopy is the measurement of a property as a function of wavelength or frequency. Time-resolved measurements were used in order to find out the characteristic timescales of the photo-induced processes. The time-correlated single photon counting (TCSPC) method is described here in more detail. The principal difference of the time-resolved fluorescence (or absorbance) methods lies not in the measured quantity, but in the technical implementation of the measurement.

3.3.1 Steady-state absorption and emission spectroscopy

Spectroscopic steady-state measurements for all the synthesized compounds were carried out with a conventional UV-Vis absorption spectrophotometer in the 300-800 nm range. The absorption spectra were used to monitor the effect of various substituents on the parent derivatives. Furthermore, the absorption spectra were used to select the excitation wavelengths for the steady-state fluorescence measurements and the time-resolved measurements. The absolute value of the absorbance (A) of a known concentration solution was used to calculate the molar extinction coefficient (ε) via the Beer-Lambert law: $A = \varepsilon c l$,[126] where c is the molar concentration of the solution and l is the length of the light path. The absorption spectra also provided a way to verify the film thickness in conjugation with profilometer measurements for buffer layer deposition.[II]

Steady-state fluorescence measurements were performed with a continuous excitation and the emission intensity was followed in the 400-800 nm range. Fluorescence measurements were used to detect the effect of various substituents on the parent derivatives and were also used to calculate the quantum yield of the solution using a reference dye.

3.3.2 Time-correlated single photon counting (TCSPC)

Fluorescence lifetimes on a nano-second timescale were measured using the TCSPC system. The scheme of the TCSPC measurement is shown in Figure 3.5. The sample is excited by a laser pulse, and the same laser pulse is used as a trigger pulse for the time-to-amplitude converter (TAC). The triggering pulse starts the generation of a linearly rising voltage in the TAC, and the pulse from emitted photon stops the rising potential in the TAC. The emitted photons are detected with a photomultiplier tube, which works in photon counting mode and thus produces an

electrical pulse after each detected photon. Because the rise of the TAC output voltage is linear in time, a certain output voltage corresponds to a certain delay time, Δt, between the excitation pulse and the emitted photon. The output voltage of TAC ($U(\Delta t)$) as a function of the delay time is processed by the multichannel analyzer (MCA), where each channel is associated to some voltage interval and therefore, to some delay time interval. Each output voltage value adds one to the value stored at the corresponding channel. For example, the time step of the instrument can be set to 16 ps and then each channel stores the counts at this resolution. The measurement results, after repeated excitation pulses, in a decay curve with the number of counts as a function of delay time. The time resolution of the instrument can be found out by measuring the instrument response function (that is, the decay profile of scattering of the excitation pulse). For the used setup it was ~ 100 ps. The fluorescence decays obtained from the TCSPC measurements were fitted with mono- or multi-exponential functions to obtain fluorescence lifetimes.[126]

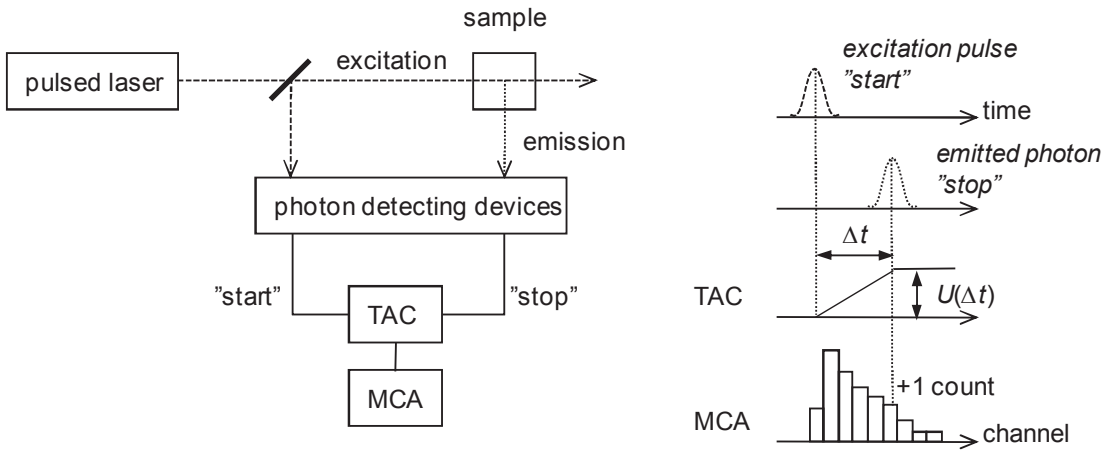

Figure 3.5. Scheme of the time correlated single photon counting (TCSPC) setup.

3.4 Differential pulse voltammetry (DPV)

Differential pulse voltammetry (DPV)[127, 128] was used to estimate the reduction and oxidation potentials of the synthesized derivatives. DPV was carried out at room temperature under high-purity nitrogen flow and recorded using a potentiostat (Iviumstat Compactstat IEC 61326 Standard) controlled by an IBM computer with the software Iviumsoft (Version 1.752) in a three-electrode single-compartment cell consisting of platinum in glass as working electrode, Ag/AgCl as reference electrode, and graphite as a counter electrode. Benzonitrile containing 0.1 M $TBABF_4$ was used as solvent. $TBABF_4$ was dried under vacuum at 110 ^{0}C for 2 h before use. All potentials were internally referenced to the ferrocene/ferrocenium (Fc/Fc^+) couple. Under these conditions, the Fc/Fc^+ couple potential was determined to be +0.48 V. The measurements were carried out in both directions: toward the positive and negative potential.

The reduction and oxidation potentials were calculated as an average of the two scans. The HOMO and the LUMO energy levels of the studied compounds were calculated by using commonly used procedure, through the equation as follows:[129]

LUMO = - (E_{1red} + 4.8) eV, in which E_{1red} is the reduction potential referenced against ferrocene;

HOMO = - (E_{1ox} + 4.8) eV, in which E_{1ox} is the oxidation potential referenced against ferrocene; or,

HOMO = (LUMO - E^{opt}_{g}) eV, in which optical band gap, $E^{opt}_{g} = 1240/\lambda_{max}$.

The value for Fc with respect to the zero vacuum level is estimated at -4.8 eV, determined from -4.6 eV for the standard electrode potential $E°$ of a normal hydrogen electrode (NHE) on the zero vacuum level, and 0.2 V for Fc vs. NHE.

3.5 Film deposition methods

The organic solar cells presented here were prepared by thin-film based technologies. The films in this work have been prepared mainly by spin-coating and vacuum thermal evaporation techniques.

3.5.1 Spin-coating

The spin-coating method is probably the easiest and fastest for thin film preparation and has been used for several decades for this purpose.[17] This procedure is typically used to apply thin films on flat substrates. A typical process involves depositing a small puddle of a solution of the desired compound or a mixture of compounds onto the center of a substrate and then spinning the substrate at high speed, generally under controlled atmosphere. Centripetal acceleration will cause the solution to spread to, and eventually off the edge of the substrate, leaving a thin film of the desired compound or mixture on the surface. Final film thickness and other properties will depend on the nature of the solution (viscosity, drying rate, percent solids, surface tension, etc.) and the parameters chosen for the spin process. Factors such as final rotational speed, acceleration, and fume exhaust contribute to how the properties of the coated films are defined. One of the most important factors in spin-coating is its repeatability. Subtle variations in the parameters that define the spin process can result in drastic variations in the coated film.

In the present study, ZnO layer and the P3HT/PCBM bulk have been deposited by spin-coating, when used as the main photoactive layer in photovoltaic devices. The ZnO layer was prepared from a zinc acetate ($Zn(OCOCH_3)_2$. $2H_2O$) solution (50 g L^{-1}) in 96 % 2-methoxyethanol and 4 % ethanolamine and was fabricated according to the literature procedure. P3HT and PCBM were dissolved separately in 1,2-dichlorobenzene, and stirred at 50 ^{0}C overnight. The solutions were subsequently combined, stirred at 70 ^{0}C for 2 h, and finally sonicated (at 50 ^{0}C for 30 min.) before the spin-coating. In the OSC devices, the total concentration of P3HT/PCBM was 32 g L^{-1} (1:0.8 weight ratios). The P3HT/PCBM blends were spin-coated (600 rpm for 5 min. in a WS-400B-6NPP/LITE spin-coater from Laurell Technologies Corporation) in an ambient air under N_2 flow. The spin-coated films were annealed at 110 ^{0}C for 10 min. in vacuum.

3.5.2 Vacuum thermal evaporation

The vacuum thermal evaporation method is a common method for both organic and inorganic thin film deposition.[18] This method can be easily used to ensure smooth thin film deposition and controllable thickness. In a typical procedure, the evaporable material is placed in a ceramic jar, or high melting metallic (molybdenum or tungsten) container in high vacuum (~ 10^{-6} mbar) and the vacuum allows the vapor particles to travel directly to the target substrate, where they condense back as thin solid films.

In this work, for organic compound evaporation a ceramic jar and for metal molybdenum, boat was used. The organic compounds, the Znb_2 complexes were heated up to specific temperatures (chosen according to their melting points). The thickness of the evaporated films was monitored with a piezoelectric microcrystal balance, where a charge in the resonance frequency of the crystal corresponds to the mass of deposition substrate. The crystals were calibrated by an optical profilometer. The reproducibility of the evaporated thickness could be easily checked through steady-state absorption spectroscopy.

The inorganic material (here, Au) has been evaporated through a shadow mask as the metal electrode (anode) for solar cells. The growth rates of all the evaporation were kept low (≤ 0.01 nm s^{-1}) during the processes.

3.6 Photocurrent measurements

After the photovoltaic samples were prepared, their current-voltage (*J-V*) characteristics were measured under dark and white-light illumination. By recording the *J-V* curves of illuminated solar cell, it is possible to determine the maximum power output, and thus the power conversion efficiency. Most of the photovoltaic parameters can be directly derived from the *J-V* characteristics, like short circuit current (J_{sc}), open circuit voltage (U_{oc}), calculated fill factor (FF), and power conversion efficiency (η). J_{sc} is the current, which flows with zero internal resistance (at V = 0, when no bias voltage is applied). U_{oc} is the voltage in the open-circuit conditions, i.e. when no current flows through the cell. The power conversion efficiency of the device (η) can be calculated from the defined parameters. η is the ratio of the generated power to the incident optical power (P_0). In the end, η is the most important parameter of any given solar cell. Hence, η can be expressed as follows (Equation 3.1):

$$\eta = \frac{P_{\max}}{P_0} = \frac{\mathrm{FF}.J_{sc}.U_{oc}}{P_0}, \tag{3.1}$$

FF is the maximum power that can be withdrawn from the device (P_{max}) and theoretical power (Equation 3.2):[18]

$$\mathrm{FF} = \frac{P_{\max}}{J_{sc}.U_{oc}} = \frac{J_{\max}.U_{\max}}{J_{sc}.U_{oc}}, \tag{3.2}$$

FF is directly related to the series and shunt resistance of the solar cell. Higher FF is desirable and corresponds to a more "square-like" shape of the *J-V* curve. Figure 3.6 shows the schematic diagram of *J-V* curves of an ideal photovoltaic device both in the dark and in a white-light illumination. In the dark, the solar cell photocurrent passing through the cell until the voltage is high enough or in other words the cell behaves like a diode. When the solar cell is illuminated, the *J-V* curve shifts downwards by the amount of photocurrent generated. The power (*P*) produced by the cell can be calculated along the *J-V* sweep by the equation $P = JU$. The power is zero at the J_{sc} and U_{oc} points, and the maximum power (P_{max}) between the two points (shaded square in Figure 3.6).

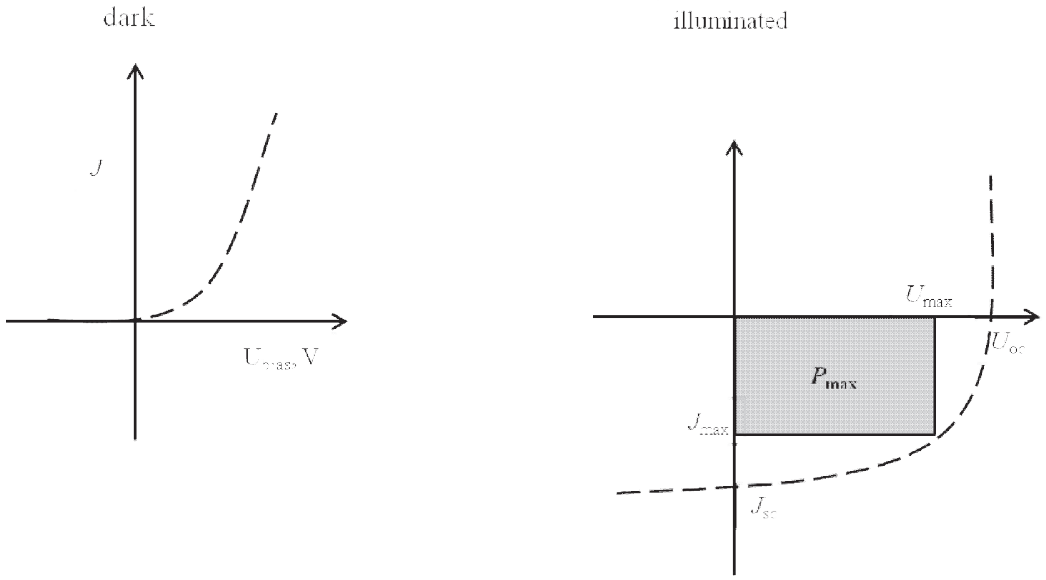

Figure 3.6. Current-voltage (*J-V*) characteristics of an ideal solar cell both in the dark (left) and under illumination (right).

In this work, the *J-V* curves were recorded in the dark and under AM 1.5 sunlight illumination. All the measurements presented in this Thesis were carried out in an open air at room temperature, without encapsulation of the devices. The solar cells were illuminated by a Xe-lamp with a filter to match the light source with the solar spectrum.

4 Results and discussion

This chapter summarizes the essential work leading up to and presented in the publications, I-IV. Firstly, the syntheses of the relevant molecules reported in publications are presented. Secondly, spectroscopic and electrochemical studies of the synthesized compounds, as well as photocurrent measurements of the solar cell samples are discussed.

4.1 Synthesis

The initial aim of the presented study was to find a way towards the tuning of photophysical properties/molecular energy levels of the zinc(benzothiazole) derivative, ultimately leading to its application in organic solar cell. The newly designed complexes were successfully used in inverted organic solar cells as anode buffer layer, and they seem to produce positive effect on the solar cell performance and long-term durability.

After having established this background, modification of the molecular energy levels of PBIs was devised by a similar approach applied for the benzothiazole derivatives. PBI derivatives are extremely important in terms of their usefulness as photo-sensitizer or acceptor in organic solar cells.

4.1.1 Zinc(benzothiazole) complexes (Znb_2)

According to the literature, photophysical properties of Znb_2 originate from the benzothiazole ligands. Theoretical computations have shown that the HOMOs are mainly localized on the phenoxide ring, the LUMOs are on the thiazolate ring of the benzothiazole ligand, and the contribution by Zn^{2+} is negligible (Figure 4.1).[130, 131] Thus, it is

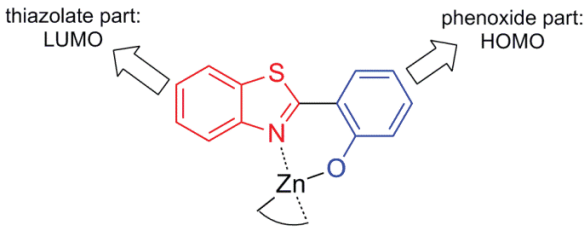

Figure 4.1. Frontier molecular orbitals of Znb_2.

possible to modify the HOMO/LUMO energy levels by simple introduction of ED/EW aryl groups to the benzothiazole ligand.

For tuning the molecular energy levels, EW/ED arenes were attached to the 5-position of the benzothiazole ligand, which ultimately modifies the HOMO energy levels and consequently, the HOMO-LUMO energy gap.

The commercial unavailability and difficult synthesis of EW-arylboronic derivatives forced to devise two different pathways for EW and ED-arenes involving the Suzuki coupling reaction. The synthetic scheme involving 5-substituted HBTs are shown in Scheme 4.1.

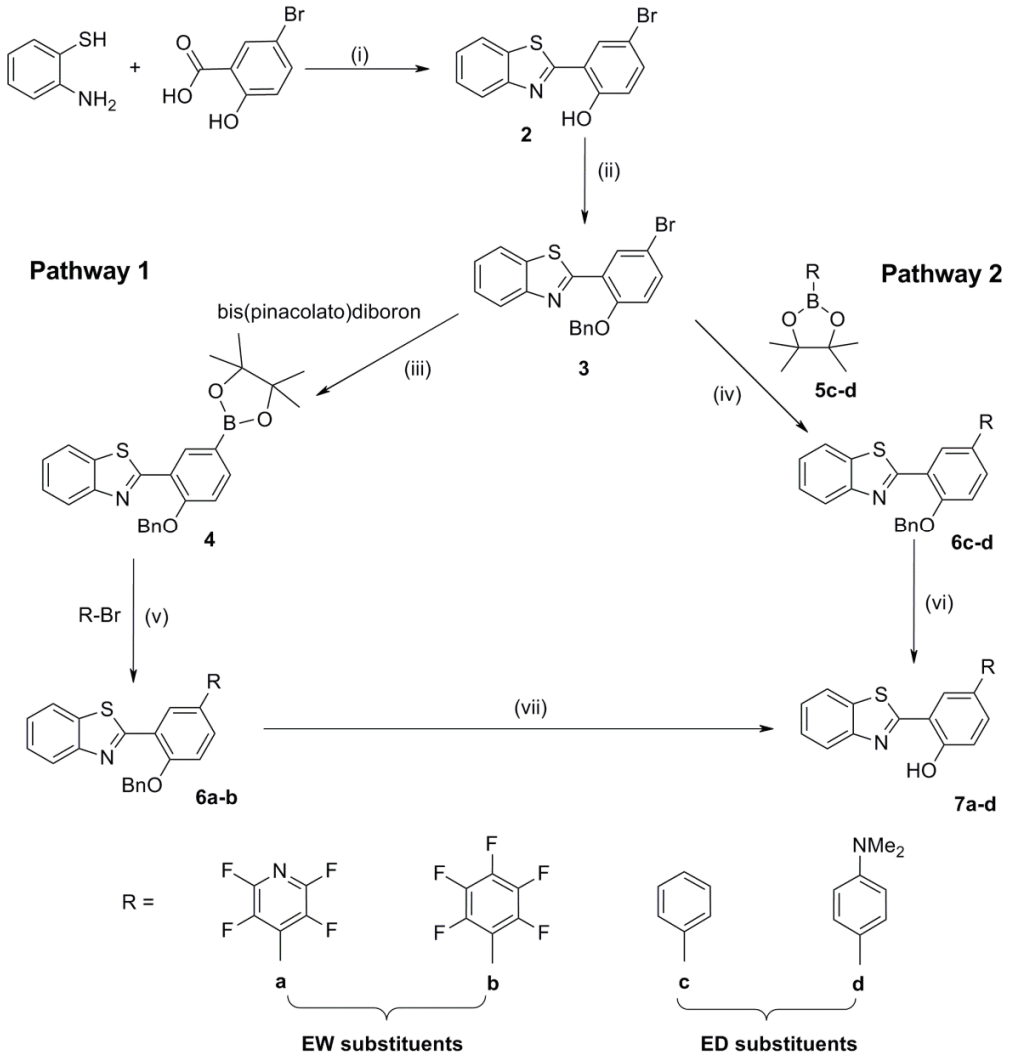

Scheme 4.1. Synthetic route to 2-(5-arylphenyl)benzothiazoles. Reagents and conditions: (i) polyphosphoric acid (PPA), 140 °C, 24 h, (ii) benzyl bromide, acetone, K_2CO_3, 60 °C, 3 h; (iii) $PdCl_2(dppf)\cdot CH_2Cl_2$, KOAc, dimethyl sulfoxide (DMSO), 80 °C, 4 h; (iv) $PdCl_2(dppf)\cdot CH_2Cl_2$, toluene, 1 M K_2CO_3, tetrabutyl ammonium chloride (TBACl), 90 °C; (v) $PdCl_2(dppf)\cdot CH_2Cl_2$, toluene, 1 M K_2CO_3, TBACl, 90 °C; (vi) Pd/C, ammonium formate (HCO_2NH_4), THF/methanol, 60 °C, 3 h; (vii) Pd/C, HCO_2NH_4 (20 eq.), tetrahydrofuran (THF), 2.0 mL water, 60 °C, 3 h.

The synthesis of HBT derivatives bearing the EW group was performed according to Pathway 1, whereas Pathway 2 was employed for the synthesis of 2-(5-arylphenyl)benzothiazoles bearing ED groups. The hydroxyl group in the starting material, 2-(5-bromo-2-hydroxyphenyl)benzothiazole **2**, was protected by a benzyl (Bn) protecting group prior to the Pd^0-catalyzed coupling reactions. The presence of strong base (here, K_2CO_3 solution) in the Suzuki coupling reaction precluded using most of the common protecting groups, except the hydrolytically stable benzyl group.

For the introduction of EW arenes, HBT **3** was converted into pinacolatoboronate ester **4** by Pd^0-catalyzed borylation in 74 % yield. This was followed by Pd^0-catalyzed Suzuki coupling with suitable EW bromoarenes, and consequent deprotection of benzyl lead to HBT **7a-b**.

For the introduction of ED arenes, HBT **3** was cross coupled with suitable ED-aryl pinacolatoboronate esters, followed by benzyl deprotection producing HBT **7c-d** in high yields.

The final $zinc^{II}$-complexes **1a-d** were obtained by reacting the deprotected ligand HBTs with $Zn(OAc)_2$ in ethanol (Scheme 4.2). The resulting complexes were purified by vacuum sublimation method and were characterized by FTIR spectroscopy and elemental analysis. The Znb_2 complexes were studied in publications I and II.

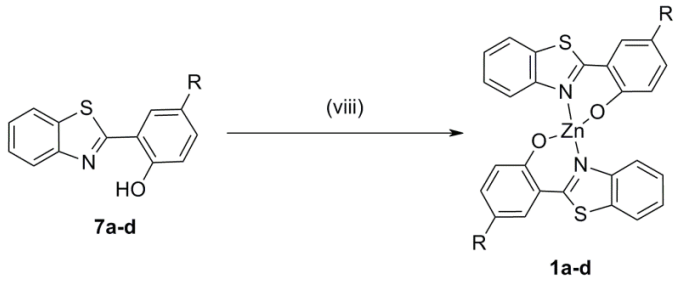

7a-d **1a-d**

Scheme 4.2. Synthetic route to zinc(benzothiazole) complex derivatives. Reagents and conditions: (viii) zinc acetate, EtOH, 70 ^{0}C; reaction times for **1a-d**: 16, 22, 36 and 48 h, respectively.

4.1.2 Borylation of benzothiazole

The borylation reaction of benzothiazole is a very important reaction as it was used to synthesize EW-aryl-substituted benzothiazoles via Suzuki coupling, as is shown in Scheme 4.3. Initially, borylation of unprotected benzothiazole **2** was considered, but even after repeated attempts; the borylation of benzothiazole remained elusive. The protection to the phenolic hydroxyl group appeared necessary, as the high acidic hydroxyl group might be deactivating the Pd catalyst. So, after protection of the hydroxyl group, borylation reaction was carried out. As standard literature method required long reaction times and gave low yields, systematic variation of the reaction condition was needed to maximize the yield of the borylated benzothiazole. The optimization conditions are shown in Table 4.1.

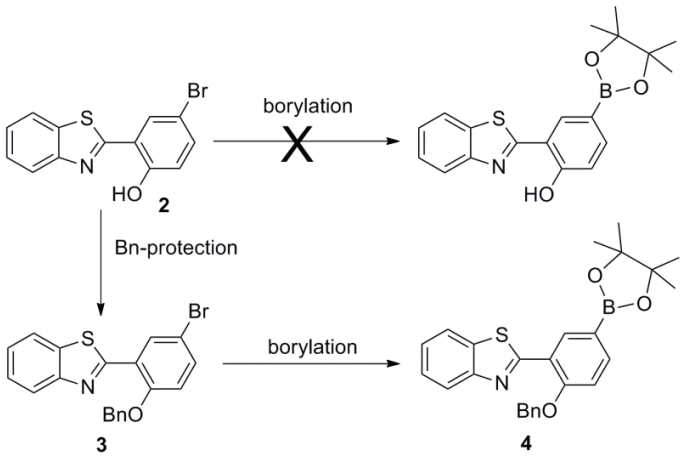

Scheme 4.3. Borylation of benzothiazole.

It was found that by using KOAc as the base, bis(pinacolato)diboron as the borylating agent, DMSO as solvent, and $PdCl_2(dppf)\cdot CH_2Cl_2$ as a catalyst at 80 ^{0}C, 4 h reaction time gave a yield of 74 % with only a small amount of side products. From the optimization studies, it is evident that a solvent with high polarity (DMSO > 1, 4-dioxane > THF > toluene) and a weak base (Et_3N > KOAc) was needed to avoid the dimerization or side reactions. The optimization of borylation reaction condition has been reported in publication I.

Table 4.1. Optimization of borylation reaction condition of benzothiazole **2**.

Entry	Base	Solvent	Catalyst	*T* [^{0}C]	Time [h]	Yield [%]
1	Et_3N[a]	dioxane	$Pd(OAc)_2$	90	24	-
2	Et_3N[a]	toluene	$Pd(OAc)_2$	110	48	11
3	Et_3N[a]	dioxane	$PdCl_2(dppf)$	90	24	17
4	Et_3N[b]	THF	$PdCl_2(dppf)$	100	36	60
5	Et_3N[a]	THF	$Pd[(PPh_3)_4]$	100	36	35
6	KOAc[b]	DMSO	$PdCl_2(dppf)$	80	24	38
7	Et_3N[a]	DMSO	$PdCl_2(dppf)$	80	12	42
8	KOAc[b]	DMSO	$PdCl_2(dppf)$	80	12	57
9	KOAc[b]	DMSO	$PdCl_2(dppf)$	80	4	74

[a] The reactions were carried out with pinacolborane. [b] The reactions were carried out with bis(pinacolato)diboron.

4.1.3 Borylation of perylene bisimide

Aryl boronic acid/esters are very useful in many organic transformations, including widely used Suzuki coupling reaction, and as there have been no reports citing the *bay* region borylation of perylene bisimide, the synthesis of PBI-boronic ester derivative was envisioned via a simple and efficient way. The effects of solvents, bases, catalysts, reaction temperatures, and times on the reaction were systematically studied. This work has been reported in publication III. The synthetic scheme is presented in Schemes 4.4 and 4.5. Borylation optimization conditions are described in Table 4.2.

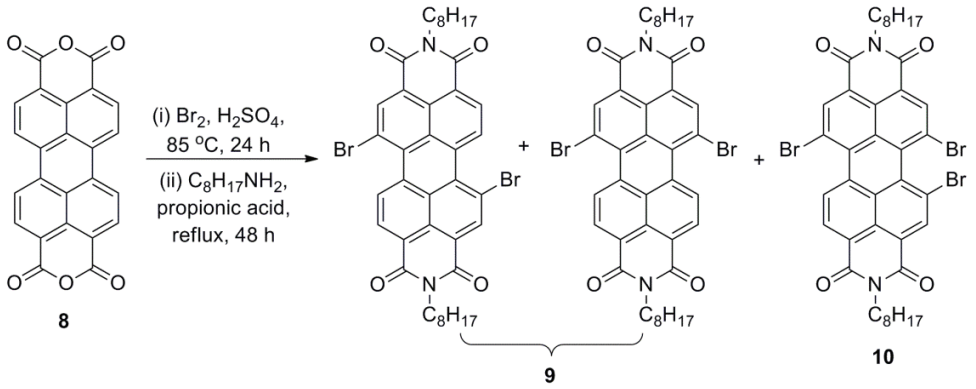

Scheme 4.4. Bromination and subsequent imidization of perylene bisanhydride **8**.

The synthesis of dibromo-PBI **9** starts with the bromination of perylene bisanhydride **8** and subsequent imidization of the bromo-PBI derivatives. As mentioned in the literature, bromination of **8** produces 1,7- and 1,6-bromo-perylene bisanhydride along with tribromo-derivatives in a very small (~ 1 %) amount.[132, 133] Unfortunately, the mixture of products cannot be separated at this stage, thus requiring imidization, and which produces a mixture of dibromo-PBI **9** and tribromo-PBI **10**. Tribromo-PBI **10** can be easily separated by silica gel column chromatography using DCM as eluent system.

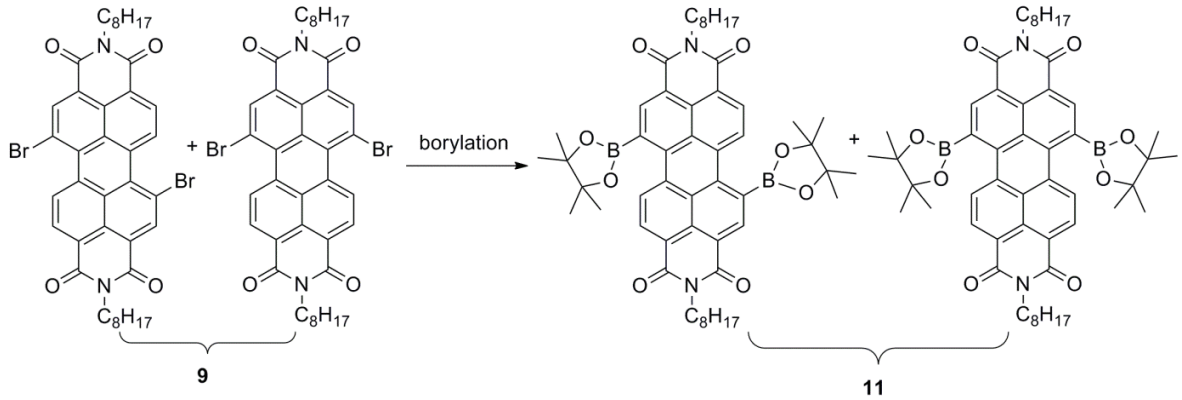

Scheme 4.5. Borylation of dibromo-PBI **9**.

However, regioisomers of dibromo-PBI could not be separated by chromatography, but 1,7-regioisomer can be isolated by repetitive recrystallization method, albeit in low yield (~ 20-25 %). Actually, presence of regioisomers can only be detected by ≥ 400 MHz ^{1}H NMR at this stage.[132] In this Thesis and in all the relevant publications, dibromo-PBI **9** was used as a mixture of regioisomers and final products were isolated as individual regioisomers.

Table 4.2. Optimization of the borylation reaction conditions of dibromo-PBI **9**.[a]

Entry	Base	Solvent	Borylating agent	*T* [°C]	Time [h]	Product A[d]	Product B[e]	Yield[f] [%]
1[b, c]	Et_3N/KOAc	DMSO	bis(pinacolato)diboron/pinacolborane	80/90/100	6-12	major	trace	0
2[b, c]	Et_3N/KOAc	dioxane	bis(pinacolato)diboron/pinacolborane	90/100	6-12	major	trace	0
3[b, c]	Et_3N/KOAc	THF	bis(pinacolato)diboron/pinacolborane	90/100	6-12	major	trace	0
4[c]	Et_3N/KOAc	toluene	bis(pinacolato)diboron/pinacolborane	90/100	6-24	major	minor	10-16
5[c]	KOAc	toluene	bis(pinacolato)diboron	110	7	major	minor	36
6[c]	KOAc	toluene	bis(pinacolato)diboron	125	12	minor	major	44
7[c]	NaOAc	toluene	bis(pinacolato)diboron	125	12	minor	major	57
8[c]	NaOAc	toluene	bis(pinacolato)diboron	125	6	minor	major	70

[a] All the reactions were performed with 8 mol % of catalyst under Ar atmosphere, [b] $Pd[(PPh_3)_4]$ as catalyst, [c] $PdCl_2(dppf)\cdot CH_2Cl_2$ as catalyst, [d] Product A was a mixture of unreacted starting material, monopinacolborane-PBI, debrominated-PBI, PBI-dimer, Pd-PBI complex etc. [e] Product B is compound **11**, [f] Isolated yield of **11**.

The *bay* region borylation of perylene bisimide is very challenging due to: (i) strong steric crowding in the *bay* region; (ii) the presence of many side products; (iii) difficult chromatographic purification of these esters on silica gel, plagued by the products sticking on the column; and (iv) stability of the product after repeated columns. After systematic variation of different reaction parameters of the borylation reaction (Table 4.2), it was found that the use of NaOAc as the base, bis(pinacolato)diboron as the borylating agent, toluene as solvent, and $PdCl_2(dppf)\cdot CH_2Cl_2$ as a catalyst at 125 ^{0}C, 6 h reaction time, and neutral alumina columns for purification gave the target bispinacolborane-PBI **11** with a yield up to 70 %. This reaction condition seemed to suppress most of the side reactions and produced the simplest columns. Unfortunately, the individual regioisomers, 1,7- and 1,6- could not be separated by chromatographic methods.

The bispinacolborane-PBI **11** was unambiguously characterized by ^{1}H NMR and HRMS methods. The ^{1}H NMR spectrum (Figure 4.2) exhibited two sets of signals with different intensities in the aromatic region between δ = 8.2-8.9 ppm, indicating the presence of 1,7- and 1,6- regioisomers. In addition, two well-resolved singlets at δ = 8.87 and 8.85 ppm and four doublets at δ = 8.63, 8.60, 8.32 and 8.27 ppm, which originate from the 2-, 5-, 8-, and 11-

perylene backbone protons, were observed. The integration of the set of singlets and the doublets revealed that 1,7- and 1,6-regioisomers were present in a ratio of 2:1.

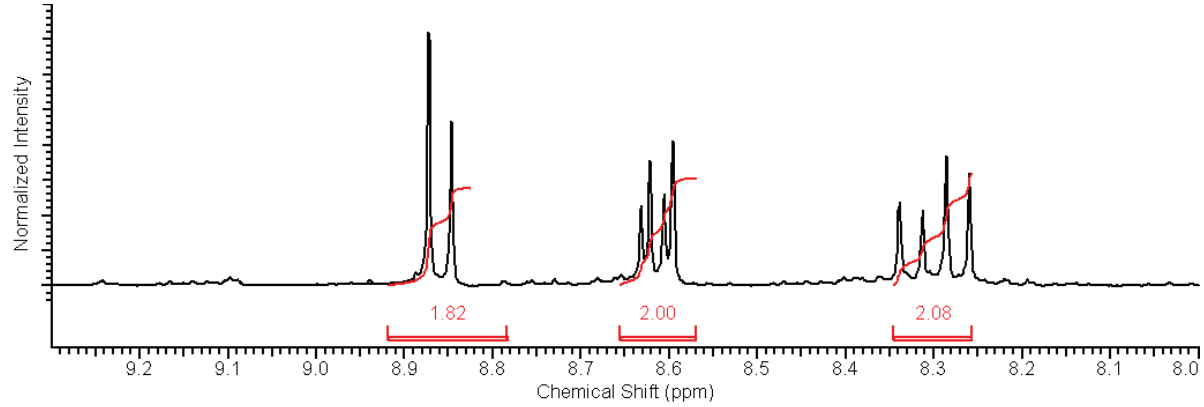

Figure 4.2. ^{1}H NMR spectrum (δ = 8.0 - 9.3 ppm) of bispinacolborane-PBI **11**.

To demonstrate the synthetic potential of newly synthesized bispinacolborane-PBI, the compounds were used in two Suzuki coupling reactions: substrates with an ED group (i.e. bromo-benzene) and with an EW group (i.e. 4-nitrobromo-benzene). These reactions produced diaryl-PBIs in high yields in both cases.

4.1.4 Perylene bisimide derivatives

The work conducted on HBT derivatives shows that it was possible to manipulate the molecular energy levels and thus, the electronic and optical properties of a molecule by attaching suitable aryl groups to the chromophore. As described in the Chapter 3.1.2, *bay* substitution is needed for effective modification of molecular energy levels of perylene bisimides. Therefore, a series of bis-substituted PBIs with ED/EW aryls were synthesized at the *bay* region of perylene. The structures of the synthesized compounds are shown in Scheme 4.6.

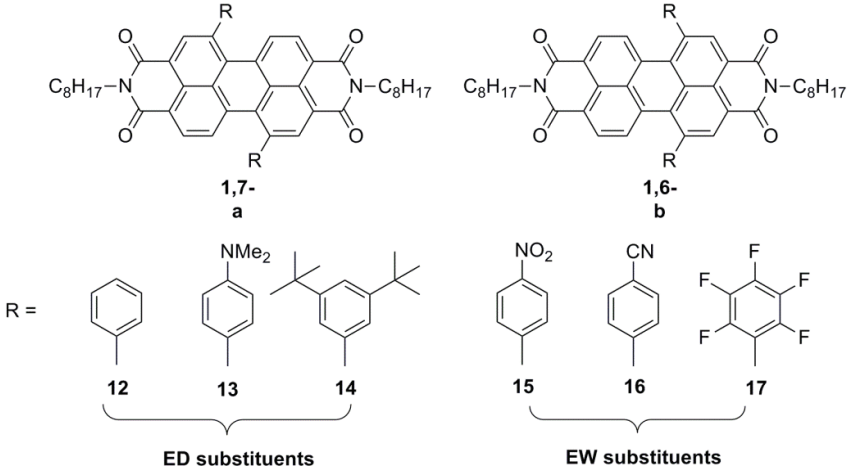

Scheme 4.6. Structures of synthesized 1,7- and 1,6-diaryl-PBIs **12-17**.

The Suzuki coupling reaction was used to attach aryl groups to the perylene core. Moreover, individual regioisomers, 1,7- and 1,6-regioisomer were isolated from the regioisomeric mixture by conventional chromatography. The isolated compounds were studied by means of spectroscopic and electrochemical methods. These results have been published in publication IV.

As EW aryl-pinacolboranes are less readily available and difficult to synthesize, two different pathways were devised to synthesize diaryl-PBIs. Scheme 4.7 was used for ED aryls, and Scheme 4.8 was used for EW aryls. The synthesis of dibromo-PBI **9** was carried out by the method described in Chapter 4.1.3 and used as a regioisomeric mixture. Pd^0 catalyzed Suzuki coupling between aryl-pinacolborane and dibromo-PBI **9** in a toluene/water biphasic system produced diaryl-PBIs **12-14** in 75-80 % yields.

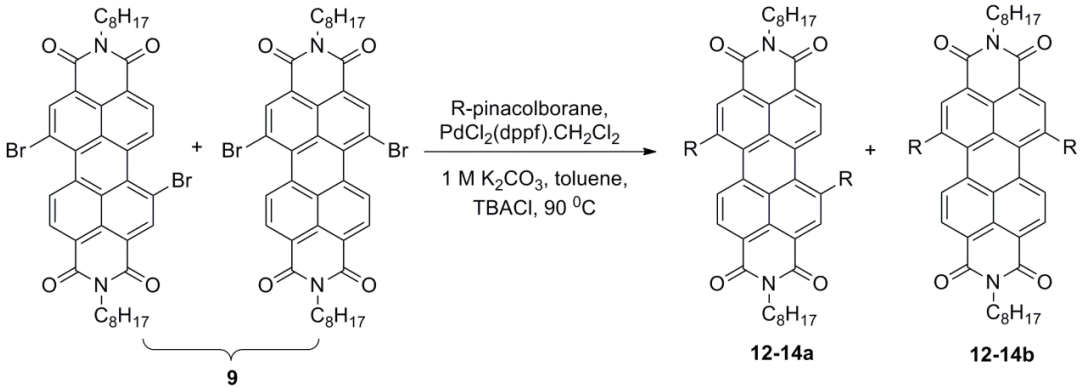

Scheme 4.7. Suzuki coupling of dibromo-PBI **9**.

The regioisomers 1,7- and 1,6- were separated by normal phase silica gel (silica 60) column chromatography in very slow running condition, normally for 2-3 days. Three separate fractions were generally collected, the first one and the last one containing pure regioisomers and the middle one a mixture of the two. The individual regioisomers were unambiguously characterized by 300 MHz ^{1}H NMR spectroscopy. Both the regioisomers produce one singlet, and two doublets for the perylene core protons, exhibiting small (< 0.2 ppm) but significant difference in the chemical shift values. However, unequivocal assignments of individual regioisomers were performed on the basis of methylene protons in *α*-position to *imide* groups, appearing at ~ 4.2 ppm. Because of the identical nature of four methylene protons, 1,7-regioisomer produced one clear triplet, whereas 1,6-regioisomer generally produced two distinct triplets (Figure 4.3 and 4.4 for Ph-PBI **12** pair). In this way, an unambiguous characterization of regioisomers has been done solely on the basis of ^{1}H NMR.

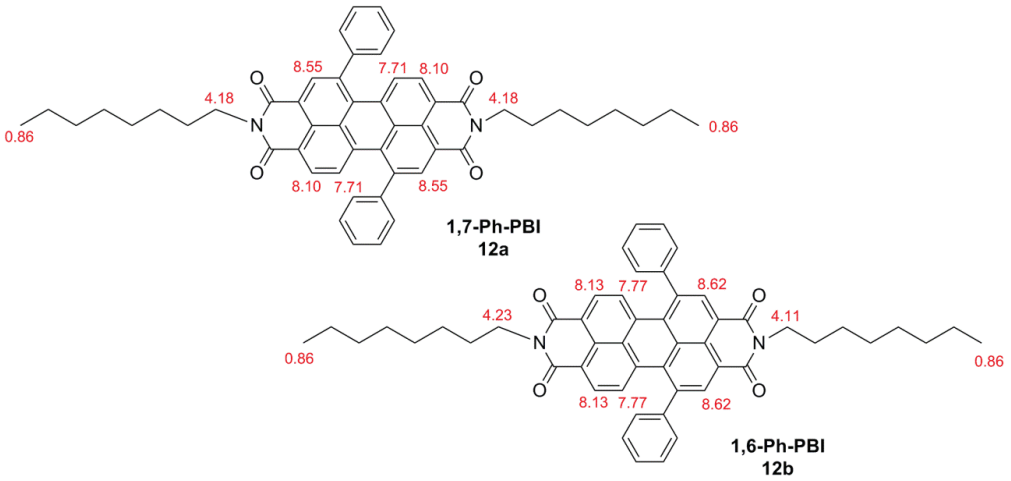

Figure 4.3. Chemical shifts of 1,7- and 1,6-regioisomers of Ph-PBI **12**.

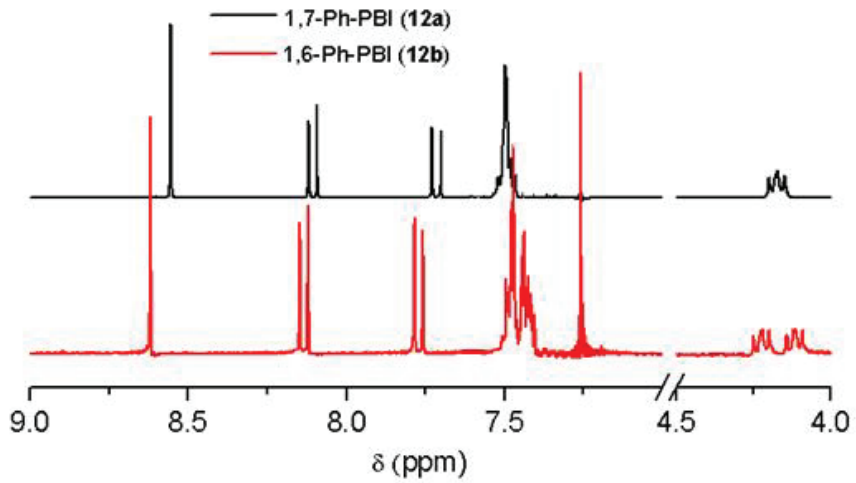

Figure 4.4. ^{1}H NMR spectra of 1,7- and 1,6-regioisomers of Ph-PBI **12**.

The syntheses of the EW diaryl-PBIs **15-17** were done by Suzuki coupling reaction between bispinacolborane-PBI **11** and aryl bromides. The synthesis of bispinacolborane-PBI **11** was described in the previous section 4.1.3. The individual regioisomer separation and characterization were done by similar methods as described for the ED diaryl-PBIs. Even after repeated attempts, the synthesis of PFP-PBI **17** was unsuccessful, presumably due to strong steric interaction between the pentafluoro phenyl group and perylene *bay* protons (Scheme 4.9). Unexpectedly, mono-PFP-PBI **18** was always isolated in high yields. The ^{1}H NMR of PBI **18** is shown in Figure 4.5.

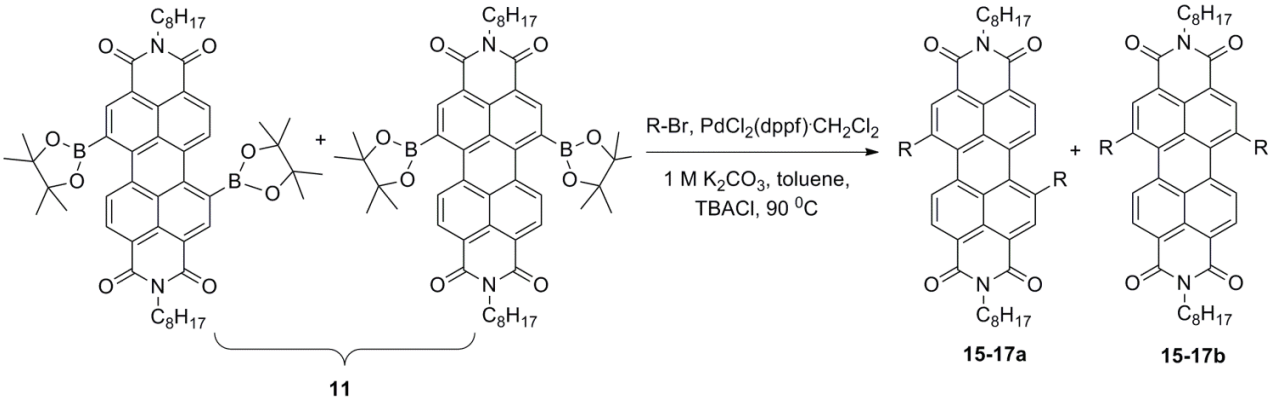

Scheme 4.8. Suzuki coupling of bispinacolborane-PBI **11**.

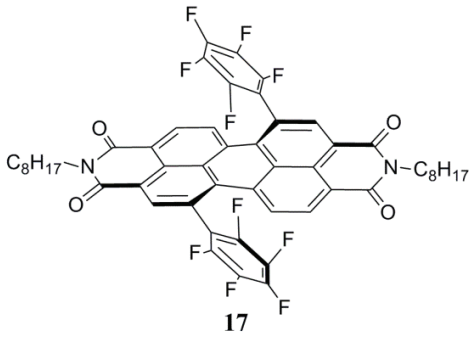

Scheme 4.9. Schematic diagram depicting strong steric interactions in PFP-PBI **17**.

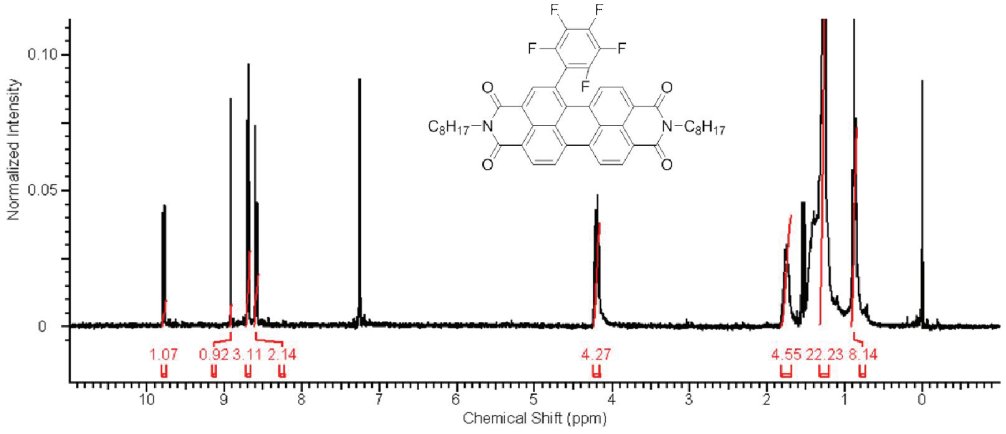

Figure 4.5. ^{1}H NMR spectrum of mono-PFP-PBI **18**.

4.1.5 Benzothiazole-perylene bisimide dyads

The syntheses of HBT-PBI **20a** and **20b** were done according to the scheme presented in Scheme 4.10. All the synthetic knowledge acquired for the publications, I, III and IV was used to synthesize the dyads.

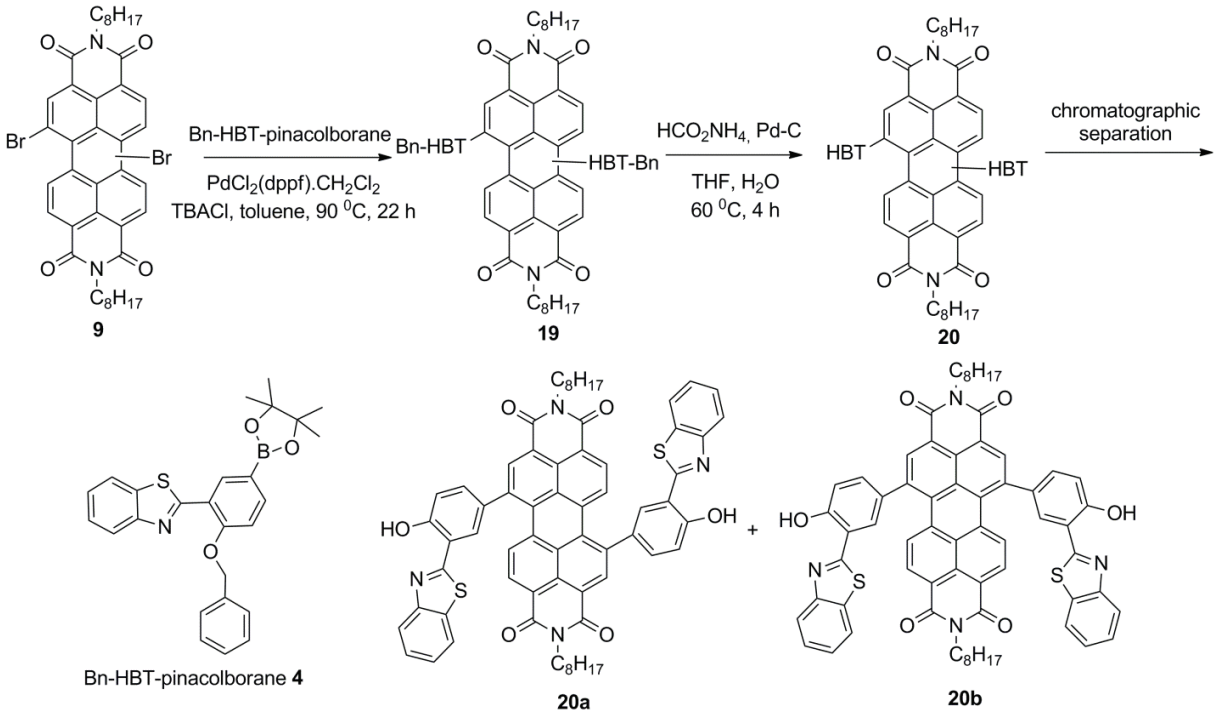

Scheme 4.10. Synthetic route to HBT-PBI dyads **20a** and **20b**.

The HBT-PBI dyads **20** can be assembled by a Pd^0 catalyzed Suzuki coupling between dibromo-PBI **9** and benzyl-protected HBT-pinacolborane **4**, followed by benzyl deprotection. The individual regioisomers were then separated by silica gel column chromatography using chloroform/hexane, 3:1 as an eluent.

The regioisomers were unambiguously characterized by ^{1}H NMR and HRMS methods. The unequivocal assignments of individual regioisomers were performed on the basis of the signal of methylene protons (in α-position to the *imide* group) which appear at ~4.2 ppm (similar to the method described in Chapter 4.1.4). For the 1,7-regioisomer, the methylene protons are equivalent and appeared as one triplet, whereas 1,6-regioisomer produced two distinct triplets for the same two methylene groups (Figure 4.6). The presence of bulky HBTs in the *bay* region of perylene seems to facilitate the separation of the regioisomers. These are unpublished results.

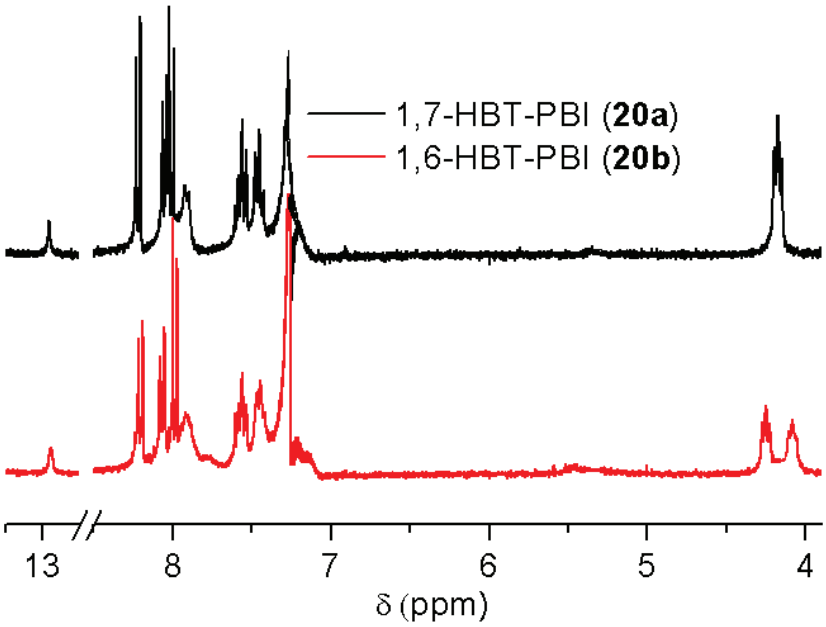

Figure 4.6. ^{1}H NMR spectra of 1,7- and 1,6-regioisomers of HBT-PBI dyads **20**.

4.2 Spectroscopic studies

Steady-state absorption and emission measurements of all the synthesized derivatives were done to visualize the effect of various substituents in comparison to the parent compounds. The spectroscopic results were part of all the manuscripts involved in this Thesis.

4.2.1 Zinc(benzothiazole) complexes

Steady-state absorption and emission spectra of all the zinc(benzothiazole) complexes were measured in chloroform and the spectroscopic parameters are presented in Table 4.3. The fluorescence quantum yields Φ_F were determined by using quinine sulphate (in 0.1 N H_2SO_4, quantum yield = 0.55) as a standard.[134] The emission spectra of the complexes **1a-d** are shown in Figure 4.7.

Table 4.3. Summarized spectroscopic parameters of the complexes **1a-d**.

Complex	λ_{max} [nm]	ε [$mol^{-1}cm^{-1}$]	λ_F [nm]	Φ_F
Znb_2	346	1.3×10^4	534	0.132
1a	337	3.1×10^4	505	0.194
1b	341	2.9×10^4	509	0.213
1c	356	1.7×10^4	556	0.111
1d	364	1.9×10^4	583	0.076

For the Znb_2 complexes bearing the EW groups **1a-b**, the π-π* absorption maximum hypsochromically shifted by 5-9 nm, whereas for the complexes with the ED group **1c-d**, the absorption maximum bathochromically shifted by 10-18 nm, compared to the parent Znb_2 complex. A similar effect can be observed for the emission maximum of the Znb_2 complexes. The emission maximum shows a considerable hypsochromic shift of 25-29 nm for the complexes **1a-b**, while bathochromic shifts of 22-49 nm were observed for the complexes **1c-d**, compared to the parent Znb_2 complex.

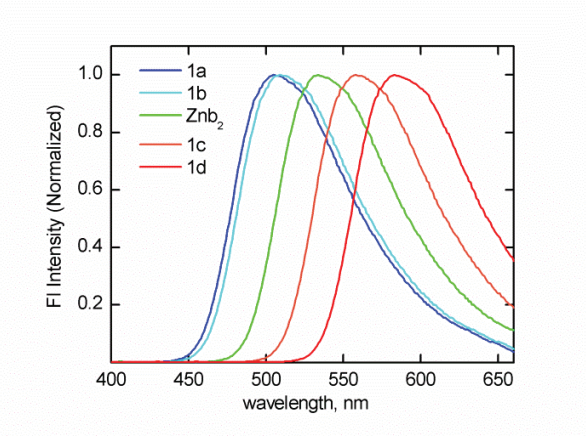

Figure 4.7. Emission spectra of the complexes **1a-d** and Znb_2 in chloroform.

From the photophysical data obtained from spectroscopic measurements of the Znb_2 complexes **1a-d**, a remarkable correlation between the photophysical properties and the electronic nature of the attached substituents was observed. It can be clearly seen that both the absorption and the emission shift systematically from blue to red depending on the electronic nature of the aryl groups. This indicates that the participation of inductive effects and reduction in the contribution from the mesomeric effect from the aryl substituents. These results were reported in publication I.

4.2.2 Perylene bisimide derivatives

All the synthesized PBIs have a high molar extinction coefficient in the solar spectrum and are green (DMA-PBI **13**) to red (Ph-PBI **12**) in color depending upon the attached aryl groups. The spectroscopic parameters are presented in Table 4.4. All the solution measurements were done in 1-2 μM chloroform solution to prevent strong perylene π-π aggregation. All the PBIs show a strong π – π* ($S_0 – S_1$) absorption band with a weaker $S_0 – S_2$ shoulder band. In comparison to the parent-PBI (dioctyl-PBI, entry 1), all the PBIs show a significant bathochromic shift of 13-125 nm along with considerable band broadening. These results could be attributed to the EW/ED inductive effect of the aryl-moieties on the perylene core and the steric core-twisting of perylene. The negative inductive effect of the 4-nitrophenyl or 4-cyanophenyl units on compound **15-16** results in a small bathochromic shift in their absorption spectra compared to other PBI derivatives. Moreover, all the regioisomeric pairs also show small but noticeable variations in the absorption spectra (Figure 4.8, for example). The molar extinction coefficient of the 1,6-regioisomer was also found to be lower than that of the 1,7-regioisomer of the same pair.

Table 4.4. Summarized spectroscopic parameters of the PBI derivatives **12-16**.

Compound	λ_{max} [nm]	ε [$mol^{-1}cm^{-1}$]	λ_F [nm]	Φ_F	τ [ns]
dioctyl-PBI	525	78600	535	1	4.32
12a (Ph)	555	42200	609	0.61	7.25
12b (Ph)	551	35400	617	0.56	6.82
13a (DMA)	481, 647	38100, 22000	-	-	-
13b (DMA)	470, 631	29400, 17300	-	-	-
14a (DTB)	561	31700	634	0.37	8.26
14b (DTB)	557	26600	641	0.35	7.53
15a (NB)	544	33300	586	0.48	6.32
15b (NB)	538	31900	592	0.43	6.14
16a (BN)	546	31600	591	0.46	6.21
16b (BN)	541	33800	600	0.49	6.53

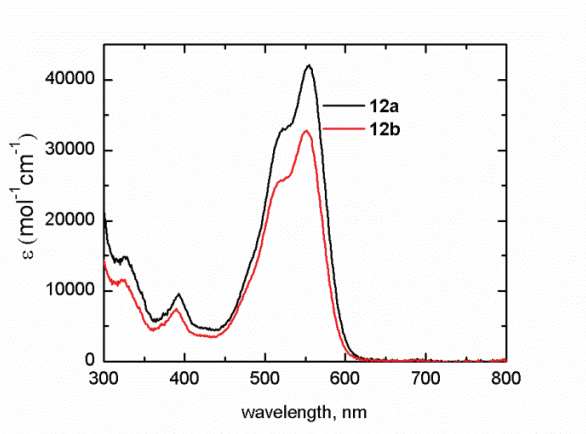

Figure 4.8. Absorption spectra of Ph-PBI **12** pair in chloroform.

All the synthesized derivatives except the DMA-PBI **13** pair are highly emissive and exhibit a broad emission profile in the 550-800 nm range and also have high fluorescence quantum yields Φ_F in the range of 0.35-0.61. The fluorescence quantum yields Φ_F were determined using fluorescein (solution in 0.1 N NaOH, quantum yield = 0.92) as a standard.[135] Emission profiles of all the PBI appear to be a mirror image of the absorption spectra with a Stokes shift of ~ 60 nm. Similar to the absorption profiles, all the regioisomeric pairs have slightly different emission spectra (Figure 4.9, for example). For 1,7-Ph-PBI **12a** the emission maxima is 609 nm and for 1,6-Ph-PBI **12b** is 617 nm.

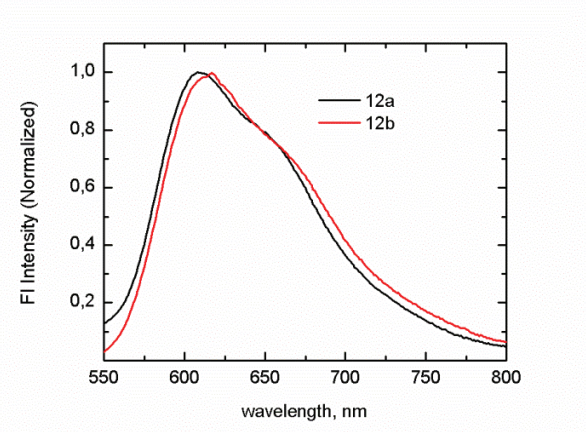

Figure 4.9. Emission spectra of Ph-PBI **12** pair in chloroform.

For the fluorescence lifetime measurements, the solutions of all the PBIs were excited at 483 nm and emission time profiles were collected at corresponding emission maximum. All PBIs show mainly mono-exponential decay with life-times (τ) of 6-9 ns. Fastest fluorescence decay was observed for PBI with the EW aryls (for **14b**, τ = 6.14 ns), whereas PBI with ED aryl showed the slowest decay (for **13a**, τ = 8.26 ns). These results have been reported in publication IV.

4.2.3 Benzothiazole-perylene bisimide dyads

The absorption spectra of the dyads and the model compounds, ref-HBT and ref-PBI (in chloroform) are shown in Figure 4.10 and the structure of the reference compounds in Figure 4.11. Structure of the dyads can be found in Scheme 4.10. The summarized spectroscopic parameters are presented in Table 4.5.

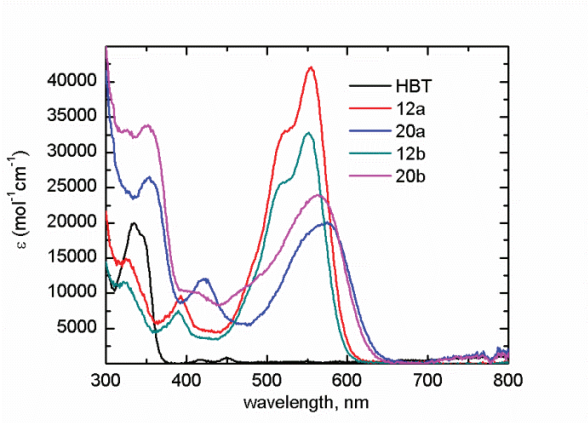

Figure 4.10. Absorption spectra of dyads, ref-HBT and ref-PBIs in chloroform.

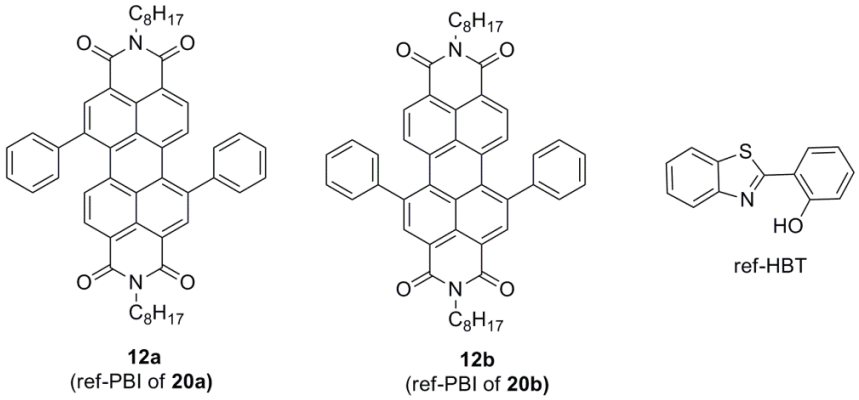

Figure 4.11. Structures of ref-PBIs and ref-HBT.

HBT strongly absorbs at wavelengths lower than 400 nm and has an absorption maximum at 341 nm. For the ref-PBIs, they exhibit absorption maxima at 555 nm and 551 nm for **12a** and **12b**, respectively. In the HBT-PBI dyads, these absorption bands are bathochromically shifted, indicating substantial ground-state electronic interactions between HBT and PBI moieties. For **20a**, absorption maxima appeared at 354 and 575 nm and for **20b**, absorption maxima appeared at 352 and 566 nm.

Table 4.5. Summarized spectroscopic parameters of the HBT-PBI dyads and the reference compounds in chloroform.

Compound	λ_{max} [nm]	ε [$mol^{-1}cm^{-1}$]	λ_F [nm]	$\tau 1$ [ns]	$\tau 2$ [ns]	$\tau 3$ [ns]
HBT	341	19700	518	0.18[a]		
12a	555	42200	609	7.25[b]		
12b	551	35400	617	6.82[b]		
20a	354, 575	26600, 20200	658	0.30[a] (45%), 0.13[b] (43%)	1.54[a] (54%), 0.92[b] (37%)	3.59[a] (1%), 2.43[b] (20%)
20b	352, 566	33900, 23900	666	0.63[a] (38%), 0.16[b] (47%)	2.47[a] (62%), 1.28[b] (53%),	

[a] λ_{ex} = 340 nm, [b] λ_{ex} = 483 nm.

The fluorescence emission spectra of the dyads and ref-compounds in chloroform are shown in Figure 4.12. Ref-HBT shows an emission maximum at 518 nm and in case of the dyads, **20a** has emission maxima at 658 nm and **20b** at 666 nm. In the case of the dyads, the emission of HBT moiety is totally quenched. The possible mechanisms of efficient quenching of HBT emission might be due to electron and/or energy transfer to the PBI unit.

For the fluorescence life-time measurements, of all the compounds were measured by excitation wavelengths of 340 and 483 nm and emission profiles were collected at 650 nm. Ref-HBT shows mono-exponential decay with a life-time of 0.18 ns, whereas ref-PBIs also show mono-exponential life-times of 7.25 ns and 6.82 ns for **12a** and **12b**, respectively. The dyads show multi-exponential decays with reduced life-time of the PBI moiety of the dyad. These results are unpublished.

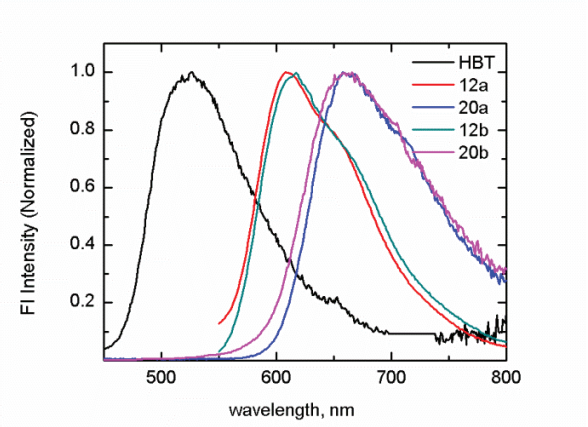

Figure 4.12. Emission spectra of dyads, ref-HBT and ref-PBIs in chloroform.

4.3 Electrochemical studies

Solution electrochemistry methods are known to provide insights into electron-transfer reactions in the condensed phase.

4.3.1 Zinc(benzothiazole) complexes

The DPV of Znb_2 complexes in solution is characterized by irreversible single oxidation and reduction processes. In order to achieve better understanding of the effect of EW/ED aryl groups on the parent Znb_2, electrochemical measurements are invaluable. The main motivation, however, was to estimate the individual HOMO and LUMO energy levels, not the energy gap of the complexes. HOMO–LUMO energy gaps were calculated from the DPV data by calibrating the scale of reference to the Fermi level. The summarized electrochemical data are presented in Table 4.6.

Table 4.6. Summarized electrochemical of Znb_2 complexes.

Complex	E_{ox} [V]	E_{red} [V]	HOMO-LUMO [eV]
Znb_2	0.90	-1.93	2.83
1a	1.16	-1.87	3.03
1b	1.12	-1.88	3.00
1c	0.83	-1.93	2.76
1d	0.56	-1.94	2.50

Interestingly, the reduction process for all the complexes was observed to remain constant at ~ -1.9 V, whereas the oxidation process took place in the 0.56-1.16 V range. It is clear from the data that the oxidation process becomes difficult for Znb_2 complexes with EW aryls, in accordance with the expected behavior of the more electron-deficient systems. Moreover, it was expected that aryl attachment might affect both the HOMO and LUMO energy levels, but the LUMO energy levels (or E_{red}) were observed to be largely unaffected throughout the series (Figure 4.13). These data have been presented in publication I.

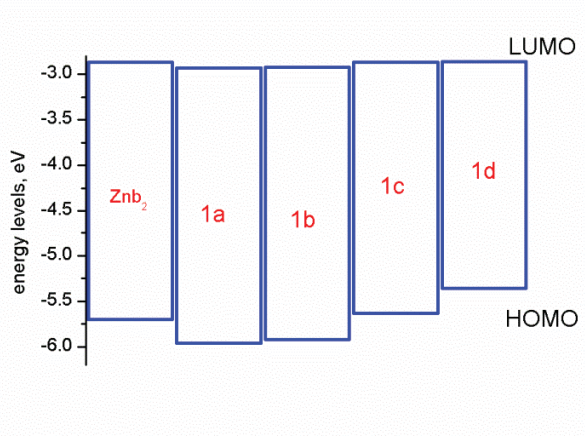

Figure 4.13. HOMO-LUMO energy levels of Znb_2 complexes.

4.3.2 Perylene bisimide derivatives

The electrochemical properties of all diaryl-PBIs were determined by the DPV method in benzonitrile containing 0.1M $TBABF_4$ as a supporting electrolyte. As the PBIs are generally considered as *n*-type organic semiconductors, i.e. electron acceptors, hence, only the measured reduction potentials and calculated HOMO and LUMO energy levels (details in Chapter 3.4) are shown in Table 4.7. All the PBIs undergo successive reversible reductions to corresponding radical anions and dianions. The reduction potentials of all the PBI derivatives are comparable to the parent PBI (dioctyl-PBI, E_{1red} = -1.02 V). The reduction potentials can be directly correlated to the electronic nature of the aryl (ED/EW) groups attached to the perylene *bay* region.

Table 4.7. Summarized electrochemical of PBI derivatives.

Compound	E_{1red} [V]	E_{2red} [V]	HOMO [eV]	LUMO [eV]	E^{opt}_g [eV]
dioctyl-PBI	-1.02	-1.23	-6.12	-3.78	2.36
12a (Ph)	-1.08	-1.28	-5.99	-3.72	2.33
12b (Ph)	-1.11	-1.32	-5.95	-3.69	2.25
13a (DMA)	-1.15	-1.35	-5.56	-3.65	1.91
13b (DMA)	-1.13	-1.33	-5.63	-3.67	1.96
14a (DTB)	-1.12	-1.32	-5.89	-3.68	2.21
14b (DTB)	-1.14	-1.35	-5.88	-3.66	2.22
15a (NB)	-0.91	-1.18	-6.16	-3.89	2.27

15b (NB)	-0.94	-1.20	-6.16	-3.86	2.30
16a (BN)	-0.94	-1.19	-6.12	-3.86	2.26
16b (BN)	-0.96	-1.21	-6.13	-3.84	2.29

The reduction potentials of ED diaryl-PBIs are higher (E_{1red} = -1.16 V for **13a**) than those of EW diaryl-PBIs (E_{1red} = -0.91 V for **15a**). Their lees negative reduction potentials mean that they are behaving as strong electron acceptors. The systematic variations of the reduction potentials indicate the strong inductive influence of ED/EW aryl groups on PBIs. It is also evident that all the corresponding regioisomeric pair has slightly different reduction potentials, which suggests that this property can be accentuated when designing materials for optical devices. The calculated HOMO energy levels are in the range of -6.16 to -5.55 eV and LUMO energy levels are -3.89 to -3.64 eV (Figure 4.14). These data have been reported in publication IV.

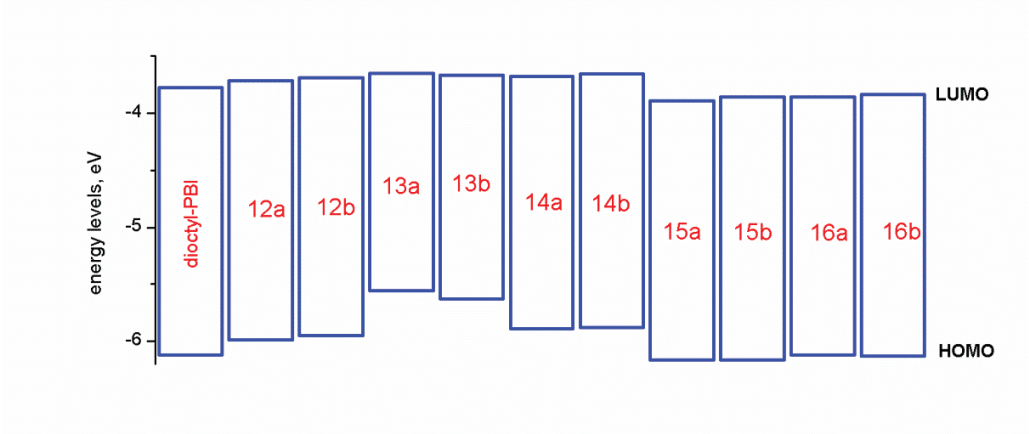

Figure 4.14. HOMO-LUMO energy levels of PBI derivatives.

4.4 Photocurrent experiments

The synthesized Znb_2 complexes **1a-d** were used as an anode buffer layer in P3HT/PCBM blend based inverted OSCs. The use of Znb_2 complexes proved to be important both in terms of improved device performance and long-term device stability in ambient air conditions. All the photocurrent measurements can be found in publication II.

4.4.1 Influence of buffer layer on organic solar cell performance

Summarized current-voltage (*J-V*) parameters of the prepared devices under white-illumination with an intensity 50 mW cm^{-2} are shown in Table 4.8 and the *J-V* characteristics in Figure 4.15. In the prepared devices, both the electrodes work-functions have been modified by introduction of ZnO on the ITO cathode and Znb_2 complexes on

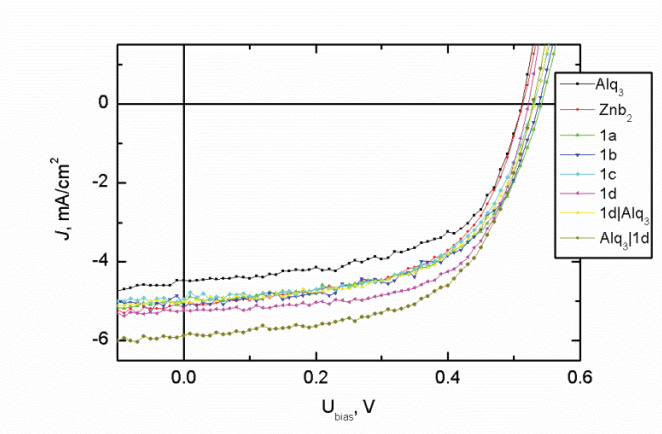

Figure 4.15. *J-V* characteristics for the studied devices with different buffer layers.

the Au anode side, respectively. This favors electron transport from Au (-5.1 eV) towards ITO (-4.7 eV). Moreover, the ZnO layer used as HBL in the inverted OSC devices [46, 64] and the Au anode improved device stability.[136] By comparing the photovoltaic parameters of the devices containing no buffer layer or Alq_3 with Znb_2 complexes as a buffer layer, it is clear that the introduction of Znb_2 buffer layers are beneficial to the improved device performance. In all the examples, J_{sc} was improved by 14-33 % and η were improved by 14-41 % when switching from Alq_3 to Znb_2 buffer layer devices. In the prepared devices, the Znb_2 buffer layers seem to be playing multiple roles as: (i) hole-transporting layer; (ii) exciton blocking layer; (iii) modifier of Au work-function; and (iv) encapsulation of the finished devices.

Table 4.8. Summary of the photovoltaic parameters (measured one day after the Au evaporation) for devices containing different buffer layers.

Sample	Buffer layer	J_{sc} [mA/cm^{-2}]	U_{oc} [V]	FF	η [%]
1	no buffer	3.57	0.47	0.55	2.08
2	Alq_3	4.45	0.49	0.59	2.77
3	Znb_2	5.05	0.52	0.60	3.14
4	**1a**	5.03	0.54	0.61	3.33
5	**1b**	5.13	0.53	0.60	3.30
6	**1c**	5.01	0.53	0.61	3.26
7	**1d**	5.22	0.55	0.64	3.55
8	**1d**|Alq_3	5.02	0.52	0.61	3.31
9	Alq_3|**1d**	5.87	0.53	0.62	3.90

The energy-level diagram illustrating the molecular energy levels of active layers, together with electrode work-functions are presented in Figure 4.16.[32, 46] Of all the Znb_2 complexes, **1d** works best in OSC devices (entry 7), as the HOMO energy level of **1d** (-5.36 eV) has a negligible difference, both with the HOMO level of P3HT (-5.2 eV) and the Au work-function (-5.1 eV) which favors efficient hole movement towards the Au anode, resulting in improved J_{sc} up to 5.22 mA cm^{-2}, U_{oc} of 0.55 V and FF of 0.64. Moreover, the introduction of double buffer layer "Alq_3|**1d**" (entry 9) increased the J_{sc} further up to 5.87 mA cm^{-2}, producing an η of 3.90 %.

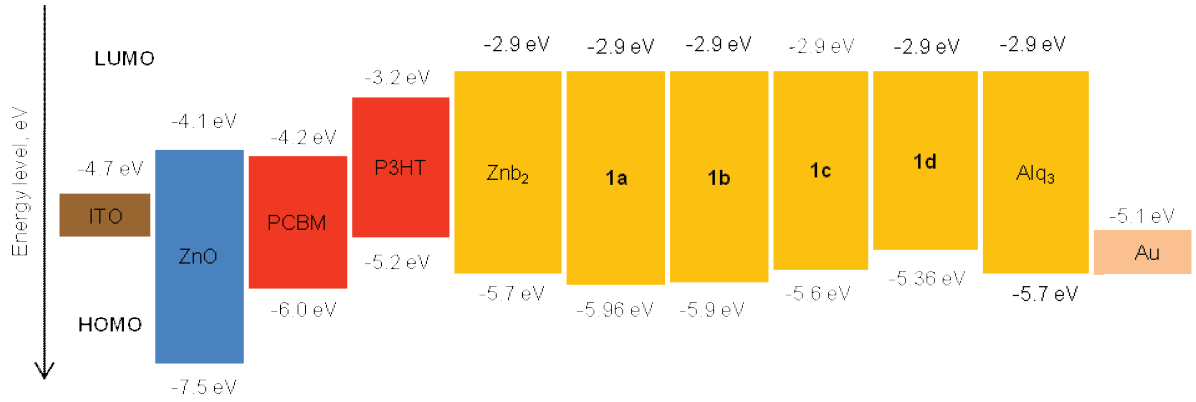

Figure 4.16. Energy-level diagram illustrating the HOMO-LUMO energy levels of the active materials and the work-function of the electrodes.

4.4.2 Stability of organic solar cells

The stability of the prepared devices was tested for a total period of 245 days, and different photovoltaic parameters calculated from the *J-V* curved were plotted as a function of time (expressed in days), as shown in Figure 4.17. As the individual photovoltaic parameters describe how the photovoltaic device converts incident photons into electricity, one can get a clearer picture of the device degradation by plotting those parameters against function of time. All the photovoltaic parameters were normalized to their initial value.

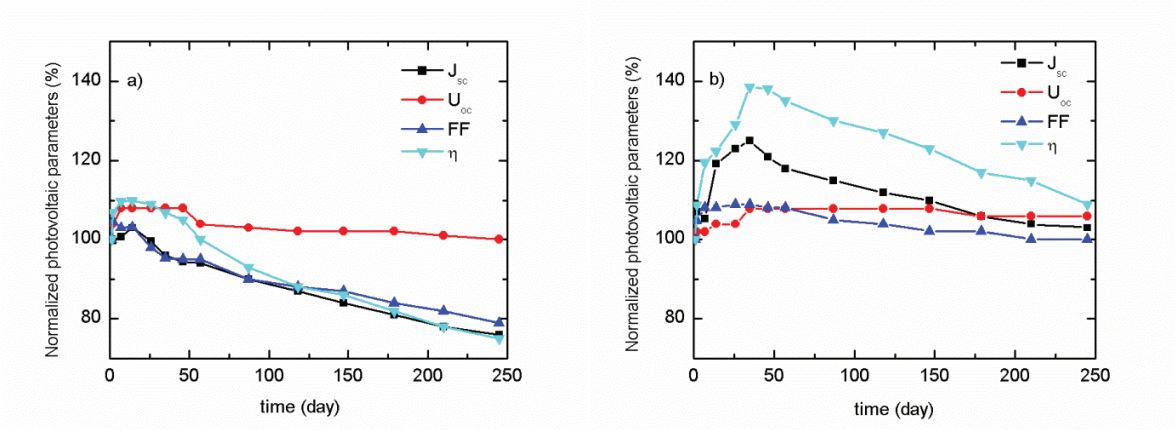

Figure 4.17. Normalized photovoltaic parameters plotted as a function of time (in days) for the device containing Alq_3 (a) and **1d** (b) as buffer layer.

By comparing the device containing the Alq_3 buffer layer with the **1d** derivative buffer layer, it is evident that Znb_2 buffer layers not only prevent the long-term device degradation, but also improve the device performance on short-terms basis (for **1d**, η improved up to 138 % after 35 days). The improved device stability is presumably due to better encapsulation of the active layers (P3HT/PCBM) from water vapor or oxygen in the atmosphere, which generally have a detrimental effect on the device stability.[26] The reproducibility of the described degradation trends was verified by investigating several devices with an identical structure.

4.5 Future perspectives

The results achieved with this work provide a relevant step towards the realization of thin film solar cells. OSCs have an unlimited number of potential applications because of their possibility of being thin, flexible, and cheap. The first attempts to build devices for electricity generation can pave the way for the development of thin film OSC devices. Moreover, initial studies show that it is possible to fabricate OSCs with lifetimes of almost one year or more. Nevertheless, few issues are still left open, mainly concerning the performance of the fabricated photovoltaic devices.

The highest power conversion efficiency presented in this work was 3.90 % for an ITO|ZnO|P3HT/PCBM|Alq_3|**1d**|Au cell.[III] The efficiency value lies in the average range of performance typically obtained for polymer/PCBM blend based BHJs. It should be mentioned that the main aim of the study is to offer a novel buffer layer for inverted OSC devices with an improved device lifetime without encapsulation. The main weaknesses of the investigated OSC come from the fact that: (i) P3HT absorbs only in 400-600 nm spectral range, which is not ideal for making highly efficient OSCs; and (ii) low total absorption (absorbance ~ 0.7) of OSCs. Hence, for high-performing OSC, we required to have: (i) broad and strong absorption band for active materials in visible and NIR region to match solar spectrum; (ii) relatively low-lying polymer HOMO level; and (iii) high charge carrier mobility for both polymer and acceptor.

5 Conclusions

The main results of this Thesis are summarized as follows:

1. The synthesis, spectroscopic and electrochemical measurements of a series of 5-substituted Znb_2 complexes with EW/ED aryl group was studied. Two separate pathways based on Suzuki coupling were devised to carry out the synthesis of complexes of a diverse electronic nature in a simple and efficient fashion. Moreover, standardization of the reaction conditions of both the borylation of protected-HBT and the Suzuki coupling reactions were done systematically.

From the optical studies, it was shown that EW/ED substituents exert a systematic tuning effect on the Znb_2 complexes. Complexes bearing EW groups show hypsochromic shifts in both the absorption and emission spectra, whereas complexes bearing ED groups show bathochromic shifts. Moreover, from the calculated molecular energy levels, it was demonstrated that the HOMO levels were effectively manipulated, while the LUMO levels were largely unaffected for all the synthesized complexes (results from Chapter 4.1.1, 4.1.2, 4.2.1 and 4.3.1).

2. The synthesized Znb_2 complexes were successfully used as an anode buffer layer in P3HT/PCBM blend based inverted OSC devices. The performance and lifetime of the devices were compared with the devices containing Alq_3 buffer layer or no buffer layer. The power conversion efficiency was improved up to 30 % for single buffer layer **1d** and up to 40 % with the double buffer layer Alq_3|**1d**. The improved performance correlates with the better alignment of the HOMO levels of Znb_2 complexes both with the HOMO of P3HT and Au work-function.

The stability of the devices was studies in a time frame of 245 days. Even though, from fabrication to storage, the devices were handled in the open atmosphere without any encapsulation, the stability of the devices was excellent compared to Alq_3 buffer layer solar cells (results from Chapter 4.4).

3. Bispinacolborane-PBIs were synthesized in high yield. The use of mild base, a non-polar solvent, and a high reaction temperature proved to be essential for the successful synthesis, as they prevent numerous side reactions. Moreover, two successful Suzuki couplings of the bispinacolborane-PBI demonstrated the applicability of the newly synthesized target compound (results from Chapter 4.1.3).

4. A series of diaryl-substituted-PBIs bearing ED/ED groups were synthesized via the Suzuki coupling reaction. The two individual regioisomers, 1,7- and 1,6- were isolated via conventional silica gel column chromatography without any recrystallization. The individual regioisomers were unambiguously characterized by 300MHz ^{1}H NMR via pattern of *α-imide* protons.

All the PBIs were studied extensively by spectroscopic and electrochemical methods. The opto-electrochemical properties of 1,7- and 1,6- regioisomers of a particular pair were found to be little different from each other. Moreover, the optical and electrochemical properties of PBI derivatives varied systematically in accordance with the electronic nature of the attached aryl groups (results from Chapter 4.1.4, 4.2.2 and 4.3.2).

5. The synthesis of the HBT-PBI dyads was done via a simple yet efficient Suzuki coupling reaction. The 1,7- and 1,6-regioisomers were separated by conventional column chromatography. Initial spectroscopic studies indicate that there might be energy and/or electron transfer from the HBT moiety to the perylene (results from Chapter 4.1.5 and 4.2.3).

6 References

[1] "BP Energy Outlook 2030", http://www.bp.com/sectiongenericarticle800.do?categoryId=9037134&contentId=7068677.

[2] Potočnik, J., *Science* **2007**, *315*, 810-811.

[3] "Greenhouse Gases - EPA", http://www.epa.gov/climatechange/indicators/pdfs/CI-greenhouse-gases.pdf.

[4] "Climate Change and Water - IPCC". http://www.ipcc.ch/publications_and_data/publications_and_data_technical_papers.shtml.

[5] Hagfeldt, A., Boschloo, G., Sun, L., Kloo, L., Pettersson, H., *Chem. Rev.* **2010**, *110*, 6595-6663.

[6] "Renewable 2011 global status report", **2011**, http://www.ren21.net/Portals/97/documents/GSR/REN21_GSR2011.pdf.

[7] Ecole des Mines de Paris / Armines, **2006**.

[8] Morton, O., *Nature* **2006**, *443*, 19-22.

[9] Miyaura, N., Suzuki, A., *Chem. Rev.* **1995**, *95*, 2457-2483.

[10] Suzuki, A., *Chem. Soc. Rev.* **2011**, *40*, 5068-5083.

[11] Becquerel, A. E., *Compt. Rend .Acad. Sci* **1839**, *9*, 145-149.

[12] Chapin, D., Fuller, C., Pearson, G., *J. Appl. Phys.* **1954**, *25*, 676-677.

[13] Green, M. A., Emery, K., Hishikawa, Y., Warta, W., *Prog. Photovoltaics Res. Appl.* **2011**, *19*, 84-92.

[14] Geisz, J., Friedman, D., Ward, J., Duda, A., Olavarria, W., Moriarty, T., Kiehl, J., Romero, M., Norman, A., Jones, K., *Appl. Phys. Lett.* **2008**, *93*, 123505-123507.

[15] Tao, C. S., Jiang, J., Tao, M., *Sol. Energy Mater. Sol. Cells* **2011**, *95*, 3176-3180.

[16] Brabec, C. J., Dyakonov, V., Scherf, U., *Organic photovoltaics: materials, device physics, and manufacturing technologies*, Vch Verlagsgesellschaft Mbh **2008**.

[17] Brabec, C. J., *Sol. Energy Mater. Sol. Cells* **2004**, *83*, 273-292.

[18] Sun, S. S., Sariciftci, N. S., *Organic photovoltaics: mechanism, materials, and devices*, CRC **2005**.

[19] Green, M. A., *Prog. Photovoltaics Res. Appl.* **2011**,.

[20] Service, R., *Science* **2011**, *332*, 293.

[21] O'regan, B., Gratzel, M., *Nature* **1991**, *353*, 737-740.

[22] Dimroth, F., Kurtz, S., *MRS Bull.* **2007**, *32*, 230-235.

[23] Gur, I., Fromer, N. A., Geier, M. L., Alivisatos, A. P., *Science* **2005**, *310*, 462-465.

[24] Mayer, A. C., Scully, S. R., Hardin, B. E., Rowell, M. W., McGehee, M. D., *Mater. Today* **2007**, *10*, 28-33.

[25] Kippelen, B., Brédas, J. L., *Energy Environ. Sci.* **2009**, *2*, 251-261.

[26] Jørgensen, M., Norrman, K., Krebs, F. C., *Sol. Energy Mater. Sol. Cells* **2008**, *92*, 686-714.

[27] Voroshazi, E., Verreet, B., Aernouts, T., Heremans, P., *Sol. Energy Mater. Sol. Cells* **2011**, *95*, 1303-1307.

[28] Song, Q., Li, F., Yang, H., Wu, H., Wang, X., Zhou, W., Zhao, J., Ding, X., Huang, C., Hou, X., *Chem. Phys. Lett.* **2005**, *416*, 42-46.

[29] Hänsel, H., Zettl, H., Krausch, G., Schmitz, C., Kisselev, R., Thelakkat, M., Schmidt, H. W., *Appl. Phys. Lett.* **2002**, *81*, 2106-2108.

[30] Hauch, J. A., Schilinsky, P., Choulis, S. A., Childers, R., Biele, M., Brabec, C. J., *Sol. Energy Mater. Sol. Cells* **2008**, *92*, 727-731.

[31] Brabec, C. J., Dyakonov, V., Scherf, U., *Organic photovoltaics*, Wiley Online Library **2003**.

[32] Thompson, B. C., Fréchet, J. M. J., *Angew. Chem. Int. Ed.* **2008**, *47*, 58-77.

[33] Brédas, J. L., Norton, J. E., Cornil, J., Coropceanu, V., *Acc. Chem. Res.* **2009**, *42*, 1691-1699.

[34] Clarke, T. M., Durrant, J. R., *Chem. Rev.* **2010**, *110*, 6736-6767.

[35] Peumans, P., Yakimov, A., Forrest, S. R., *J. Appl. Phys.* **2003**, *93*, 3693-3723.

[36] Brédas, J. L., Cornil, J., Heeger, A. J., *Adv. Mater.* **1996**, *8*, 447-452.

[37] Tang, C. W., *Appl. Phys. Lett.* **1986**, *48*, 183-185.

[38] Hoppe, H., Sariciftci, N. S., *J. Mater. Res.* **2004**, *19*, 1924-1945.

[39] Yu, G., Gao, J., Hummelen, J., Wudl, F., Heeger, A., *Science* **1995**, *270*, 1789-1791.

[40] Halls, J., Walsh, C., Greenham, N., Marseglia, E., Friend, R., Moratti, S., Holmes, A., *Nature* **1995**, *376*, 498-500.

[41] Scharber, M. C., Mühlbacher, D., Koppe, M., Denk, P., Waldauf, C., Heeger, A. J., Brabec, C. J., *Adv. Mater.* **2006**, *18*, 789-794.

[42] Cai, W., Gong, X., Cao, Y., *Sol. Energy Mater. Sol. Cells* **2010**, *94*, 114-127.

[43] Dang, M. T., Hirsch, L., Wantz, G., *Adv. Mater.* **2011**, *23*, 3597-3602.

[44] Shaheen, S. E., White, M. S., Olson, D. C., Kopidakis, N., Ginley, D. S., *Solar and Alternative Energy,* http://spie.org/x14269.xml **2007**.

[45] Chen, L. M., Hong, Z., Li, G., Yang, Y., *Adv. Mater.* **2009**, *21*, 1434-1449.

[46] White, M., Olson, D., Shaheen, S., Kopidakis, N., Ginley, D. S., *Appl. Phys. Lett.* **2006**, *89*, 143517-143517-3.

[47] Zhao, D. W., Kyaw, A. K. K., Sun, X. W., *Energy Efficiency and Renewable Energy Through Nanotechnology* **2011**, 115-170.

[48] Liu, F., Nunzi, J. M., *Appl. Phys. Lett.* **2011**, *99*, 063301-063303.

[49] De Jong, M., Van IJzendoorn, L., De Voigt, M., *Appl. Phys. Lett.* **2000**, *77*, 2255.

[50] Gust, D., Moore, T. A., Moore, A. L., *Acc. Chem. Res.* **2001**, *34*, 40-48.

[51] Guldi, D. M., Zilbermann, I., Gouloumis, A., Vázquez, P., Torres, T., *J. Phys. Chem. B* **2004**, *108*, 18485-18494.

[52] Cheng, Y. J., Yang, S. H., Hsu, C. S., *Chem. Rev.* **2009**, *109*, 5868-5923.

[53] Spanggaard, H., Krebs, F. C., *Sol. Energy Mater. Sol. Cells* **2004**, *83*, 125-146.

[54] Anthony, J. E., Facchetti, A., Heeney, M., Marder, S. R., Zhan, X., *Adv. Mater.* **2010**, *22*, 3876-92.

[55] Kroto, H. W., Heath, J. R., O'Brien, S. C., Curl, R. F., Smalley, R. E., *Nature* **1985**, *318*, 162-163.

[56] Allemand, P., Koch, A., Wudl, F., Rubin, Y., Diederich, F., Alvarez, M., Anz, S., Whetten, R., *J. Am. Chem. Soc.* **1991**, *113*, 1050-1051.

[57] Nalwa, H. S., *Recherche* **1997**, *67*, 02.

[58] Po, R., Carbonera, C., Bernardi, A., Camaioni, N., *Energy Environ. Sci.* **2011**, *4*, 285-310.

[59] Feng, Z., Hou, Y., Lei, D., *Renewable Energy* **2010**, *35*, 1175-1178.

[60] Ma, H., Yip, H. L., Huang, F., Jen, A. K. Y., *Adv. Func. Mater.* **2010**, *20*, 1371-1388.

[61] Brabec, C. J., Cravino, A., Meissner, D., Sariciftci, N. S., Fromherz, T., Rispens, M. T., Sanchez, L., Hummelen, J. C., *Adv. Func. Mater.* **2001**, *11*, 374-380.

[62] Brabec, C. J., Shaheen, S. E., Winder, C., Sariciftci, N. S., Denk, P., *Appl. Phys. Lett.* **2002**, *80*, 1288-1290.

[63] Li, G., Chu, C. W., Shrotriya, V., Huang, J., Yang, Y., *Appl. Phys. Lett.* **2006**, *88*, 253503-253505.

[64] Kyaw, A., Sun, X., Jiang, C., Lo, G., Zhao, D., Kwong, D., *Appl. Phys. Lett.* **2008**, *93*, 221107-221109.

[65] Zhao, Y., Xie, Z., Qu, Y., Geng, Y., Wang, L., *Syn. Metals* **2008**, *158*, 908-911.

[66] Waldauf, C., Morana, M., Denk, P., Schilinsky, P., Coakley, K., Choulis, S., Brabec, C., *Appl. Phys. Lett.* **2006**, *89*, 233517-233519.

[67] Zhou, Y., Cheun, H., Potscavage Jr, W. J., Fuentes-Hernandez, C., Kim, S. J., Kippelen, B., *J. Mater. Chem.* **2010**, *20*, 6189-6194.

[68] Zhou, Y., Li, F., Barrau, S., Tian, W., Inganäs, O., Zhang, F., *Sol. Energy Mater. Sol. Cells* **2009**, *93*, 497-500.

[69] Hau, S. K., Yip, H. L., Ma, H., Alex, K. Y. J., *Appl. Phys. Lett.* **2008**, *93*, 233304-233306.

[70] Groenendaal, L., Jonas, F., Freitag, D., Pielartzik, H., Reynolds, J. R., *Adv. Mater.* **2000**, *12*, 481-494.

[71] Chiang, W. T., Su, S. H., Lin, Y. F., Yokoyama, M., *Jpn. J. Appl. Phys.* **2010**, *49*, 04DK14-04DK14-4.

[72] Kim, J. S., Park, J. H., Lee, J. H., Jo, J., Kim, D. Y., Cho, K., *Appl. Phys. Lett.* **2007**, *91*, 112111-112113.

[73] Roncali, J., *Chem. Rev.* **1997**, *97*, 173-206.

[74] Lenes, M., Wetzelaer, G. J. A. H., Kooistra, F. B., Veenstra, S. C., Hummelen, J. C., Blom, P. W. M., *Adv. Mater.* **2008**, *20*, 2116-2119.

[75] Koster, L., Mihailetchi, V., Blom, P., *Appl. Phys. Lett.* **2006**, *88*, 093511-093513.

[76] Mihailetchi, V., Blom, P., Hummelen, J., Rispens, M., *J. Appl. Phys.* **2003**, *94*, 6849-6854.

[77] Ishii, H., Sugiyama, K., Ito, E., Seki, K., *Adv. Mater.* **1999**, *11*, 605-625.

[78] Diederich, F., *Metal-catalyzed cross-coupling reactions*, Vch Verlagsgesellschaft Mbh **1998**.

[79] Molander, G., *Catalyst components for coupling reactions*, John Wiley **2008**.

[80] Suzuki, A., *Pure Appl. Chem.* **1991**, *63*, 419-422.

[81] Matos, K., Soderquist, J. A., *J. Org. Chem.* **1998**, *63*, 461-470.

[82] Amatore, C., Jutand, A., *Acc. Chem. Res.* **2000**, *33*, 314-321.

[83] Wright, S. W., Hageman, D. L., McClure, L. D., *J. Org. Chem.* **1994**, *59*, 6095-6097.

[84] Yin, L., Liebscher, J., *Chem. Rev.* **2007**, *107*, 133-173.

[85] Suzuki, A., *J. Organometal. Chem* **1999**, *576*, 147-168.

[86] Suzuki, N., Suzuki, T., Ota, Y., Nakano, T., Kurihara, M., Okuda, H., Yamori, T., Tsumoto, H., Nakagawa, H., Miyata, N., *J. Med. Chem.* **2009**, *52*, 2909-2922.

[87] Hamachi, I., Tajiri, Y., Shinkai, S., *J. Am. Chem. Soc.* **1994**, *116*, 7437-7438.

[88] Fujita, N., Shinkai, S., James, T. D., *Chem. Asian. J.* **2008**, *3*, 1076-1091.

[89] Ishiyama, T., Murata, M., Miyaura, N., *J. Org. Chem.* **1995**, *60*, 7508-7510.

[90] Tang, C. W., Vanslyke, S. A., *Appl. Phys. Lett.* **1987**, *51*, 913-915.

[91] Kulkarni, A. P., Tonzola, C. J., Babel, A., Jenekhe, S. A., *Chem. Mater.* **2004**, *16*, 4556-4573.

[92] Hamada, Y., Sano, T., Fujii, H., Nishio, Y., Takahashi, H., Shibata, K., *Jpn. J. Appl. Phys. Part 2 Lett.* **1996**, *35*, 1339-1341.

[93] Yu, G., Yin, S., Liu, Y., Shuai, Z., Zhu, D., *J. Am. Chem. Soc.* **2003**, *125*, 14816-14824.

[94] Singh, S. P., Mohapatra, Y., Qureshi, M., Manoharan, S. S., *Syn. Metals* **2005**, *155*, 376-379.

[95] Singh, S. P., Mohapatra, Y., Qureshi, M., Manoharan, S. S., *Appl. Phys. Lett.* **2005**, *86*, 113505-113507.

[96] Sano, T., Nishio, Y., Hamada, Y., Takahashi, H., Usuki, T., Shibata, K., *J. Mater. Chem.* **1999**, *10*, 157-161.

[97] Xiao-Ming, W., Yu-Lin, H., Zhao-Qi, W., Jia-Jin, Z., Xiu-Lan, F., Yuan-Yuan, S., *Chin. Phys. Lett.* **2005**, *22*, 1797-1799.

[98] Xu, X., Liao, Y., Yu, G., You, H., Chong'an Di, , Su, Z., Ma, D., Wang, Q., Li, S., Wang, S., *Chem. Mater.* **2007**, *19*, 1740-1748.

[99] Qian, Y., Li, S., Zhang, G., Wang, Q., Wang, S., Xu, H., Li, C., Li, Y., Yang, G., *J. Phys. Chem. B* **2007**, *111*, 5861-5868.

[100] Barbatti, M., Aquino, A. J. A., Lischka, H., Schriever, C., Lochbrunner, S., Riedle, E., *Phys. Chem. Chem. Phys.* **2009**, *11*, 1406-1415.

[101] Kim, Y. H., Roh, S. G., Jung, S. D., Chung, M. A., Kim, H. K., Cho, D. W., *Photochem. Photobiol. Sci.* **2010**, *9*, 722-729.

[102] Kwon, J. E., Park, S. Y., *Adv. Mater.* **2011**, *23*, 3615-3642.

[103] Kardos, M., *Ber. Dtsch. Che. Ges* **1913**, *46*, 2048-2091.

[104] Zollinger, H., *Color chemistry: syntheses, properties, and applications of organic dyes and pigments*, Wiley-VCH **2003**.

[105] Herbst, W., Hunger, K., Wilker, G., *Industrial organic pigments: production, properties, applications*, Vch Verlagsgesellschaft Mbh **2004**.

[106] Donaldson, D., Robertson, J., White, J., *Proc. Royal Soc. London Series A. Math. Phys. Sci.* **1953**, *220*, 311-321.

[107] Würthner, F., *Chem. Commun.* **2004**, 1564-1579.

[108] Huang, C., Barlow, S., Marder, S. R., *J. Org. Chem.* **2011**, *76*, 2348-2407.

[109] Brunetti, F. G., Kumar, R., Wudl, F., *J. Mater. Chem.* **2010**, *20*, 2934-2948.

[110] Gawrys, P., Boudinet, D., Zagorska, M., Djurado, D., Verilhac, J., Horowitz, G., Pécaud, J., Pouget, S., Pron, A., *Syn. Metals* **2009**, *159*, 1478-1485.

[111] Sadrai, M., Hadel, L., Sauers, R. R., Husain, S., Krogh-Jespersen, K., Westbrook, J. D., Bird, G. R., *J. Phys. Chem.* **1992**, *96*, 7988-7996.

[112] Gvishi, R., Reisfeld, R., Burshtein, Z., *Chem. Phys. Lett.* **1993**, *213*, 338-344.

[113] Kraft, A., Grimsdale, A. C., Holmes, A. B., *Angew. Chem. Int. Ed.* **1998**, *37*, 402-428.

[114] Ego, C., Marsitzky, D., Becker, S., Zhang, J., Grimsdale, A. C., Müllen, K., MacKenzie, J. D., Silva, C., Friend, R. H., *J. Am. Chem. Soc.* **2003**, *125*, 437-443.

[115] Shibano, Y., Umeyama, T., Matano, Y., Imahori, H., *Org. Lett.* **2007**, *9*, 1971-1974.

[116] Anthony, J. E., *Chem. Mater.* **2011**, *23*, 583-590.

[117] Law, K. Y., *Chem. Rev.* **1993**, *93*, 449-486.

[118] Belfield, K. D., Bondar, M. V., Hernandez, F. E., Przhonska, O. V., *J. Phys. Chem. C* **2008**, *112*, 5618-5622.

[119] Chao, C. C., Leung, M. K., Su, Y. O., Chiu, K. Y., Lin, T. H., Shieh, S. J., Lin, S. C., *J. Org. Chem.* **2005**, *70*, 4323-4331.

[120] Würthner, F., Sautter, A., Schilling, J., *J. Org. Chem.* **2002**, *67*, 3037-3044.

[121] Jimenez, A. J., Spanig, F., Rodriguez-Morgade, M. S., Ohkubo, K., Fukuzumi, S., Guldi, D. M., Torres, T., *Org. Lett.* **2007**, *9*, 2481-2484.

[122] Gunther, H., *NMR spectroscopy*, Wiley **1994**.

[123] Balcı, M., *Basic 1H-and 13C-NMR Spectroscopy*, Elsevier Science **2005**.

[124] Keeler, J., *Understanding NMR spectroscopy*, John Wiley & Sons **2011**.

[125] Atkins, P., Paula, J. d., *Elements of Physical Chemistry*, Oxford U. P **2009**.

[126] Tkachenko, N. V., *Optical spectroscopy: methods and instrumentations*, Elsevier Science **2006**.

[127] Kounaves, S. P., *Handbook of instrumental techniques for analytical chemistry* **1997**, *20*, 712-713.

[128] Bard, A. J., Faulkner, L. R., *Electrochemical methods: fundamentals and applications*, A1bazaar **2006**.

[129] Perrin, L., Hudhomme, P., *Eur. J. Org. Chem.* **2011**, 5427-5440.

[130] Qureshi, M., Manoharan, S. S., Singh, S. P., Mahapatra, Y. N., *Solid State Commun.* **2005**, *133*, 305-309.

[131] Yang, Y., Geng, H., Shuai, Z., Peng, J., *Syn. Metals* **2006**, *156*, 1287-1291.

[132] Wurthner, F., Stepanenko, V., Chen, Z., Saha-Moller, C. R., Kocher, N., Stalke, D., *J. Org. Chem.* **2004**, *69*, 7933-7939.

[133] Dubey, R. K., Efimov, A., Lemmetyinen, H., *Chem. Mater.* **2011**, *23*, 778-788.

[134] Melhuish, W., *J. Phys. Chem.* **1960**, *64*, 762-764.

[135] Chen, Z., Baumeister, U., Tschierske, C., Wurthner, F., *Chem. Eur. J.* **2007**, *13*, 450-465.

[136] Vivo, P., Jukola, J., Ojala, M., Chukharev, V., Lemmetyinen, H., *Sol. Energy Mater. Sol. Cells* **2008**, *92*, 1416-1420.

Tampereen teknillinen yliopisto
PL 527
33101 Tampere

Tampere University of Technology
P.O.B. 527
FI-33101 Tampere, Finland

ISBN 978-952-15-2827-9
ISSN 1459-2045